

The type IIn supernova 1994W: evidence for the explosive ejection of a circumstellar envelope

Nikolai N. Chugai^{1*}, Sergei I. Blinnikov², Robert J. Cumming³, Peter Lundqvist³, Angela Bragaglia⁴, Alexei V. Filippenko⁵, Douglas C. Leonard⁶, Thomas Matheson^{5,7}, Jesper Sollerman³

¹*Institute of Astronomy, RAS, Pyatnitskaya 48, 109017 Moscow, Russia*

²*Institute for Theoretical and Experimental Physics, 117218 Moscow, Russia*

³*Stockholm Observatory, Department of Astronomy, Stockholm University, AlbaNova University Center, SE-106 91 Stockholm, Sweden*

⁴*Osservatorio Astronomico di Bologna, via Ranzani 1, 40127 Bologna, Italy*

⁵*Department of Astronomy, University of California, Berkeley, CA 94720-3411 USA*

⁶*Five College Astronomy Department, University of Massachusetts, Amherst, MA 01003-9305 USA*

⁷*Harvard-Smithsonian Center for Astrophysics, 60 Garden Street, Cambridge, MA 02138 USA*

Accepted 12 May 2004. Received 11 May 2004; in original form 29 March 2004.

ABSTRACT

We present and analyse spectra of the Type IIn supernova 1994W obtained between 18 and 203 days after explosion. During the luminous phase (first 100 days) the line profiles are composed of three major components: (i) narrow P-Cygni lines with the absorption minima at -700 km s^{-1} ; (ii) broad emission lines with blue velocity at zero intensity $\sim 4000 \text{ km s}^{-1}$; and (iii) broad, smooth wings extending out to at least $\sim 5000 \text{ km s}^{-1}$, most apparent in H α . These components are identified with an expanding circumstellar (CS) envelope, shocked cool gas in the forward post-shock region, and multiple Thomson scattering in the CS envelope, respectively. The absence of broad P-Cygni lines from the supernova (SN) is the result of the formation of an optically thick, cool, dense shell at the interface of the ejecta and the CS envelope. Models of the SN deceleration and Thomson scattering wings are used to recover the density ($n \approx 10^9 \text{ cm}^{-3}$), radial extent [$\sim (4-5) \times 10^{15} \text{ cm}$] and Thomson optical depth ($\tau_T \gtrsim 2.5$) of the CS envelope during the first month. The plateau-like SN light curve is reproduced by a hydrodynamical model and is found to be powered by a combination of internal energy leakage after the explosion of an extended pre-supernova ($\sim 10^{15} \text{ cm}$) and subsequent luminosity from circumstellar interaction. The pre-explosion kinematics of the CS envelope is recovered, and is close to homologous expansion with outer velocity $\sim 1100 \text{ km s}^{-1}$ and a kinematic age of $\sim 1.5 \text{ yr}$. The high mass ($\sim 0.4 M_{\odot}$) and kinetic energy ($\sim 2 \times 10^{48} \text{ erg}$) of the CS envelope, combined with small age, strongly suggest that the CS envelope was explosively ejected $\sim 1.5 \text{ yr}$ prior to the SN explosion.

Key words: supernovae – circumstellar matter – stars: supernovae: individual (SN 1994W)

1 INTRODUCTION

Recent studies of supernovae (SNe) have made considerable progress in our knowledge of what makes a star explode. From observations of light curves and spectra, theories of pre-supernova evolution are now better constrained than

ever. Conventional wisdom says that Type II SNe (SNe II) are caused by core collapse in massive, usually red supergiant stars. In general, theory has no trouble accounting for the main features of the spectra and light curves of these objects. However, some SNe II are remarkably different, and many of their observational properties are not yet understood.

These events, sometimes known as narrow-line Type II SNe or SNe IIn (Schlegel 1990; Filippenko 1997), show

* E-mail: nchugai@inasan.rssi.ru (NNC); robert@astro.su.se (RJC); peter@astro.su.se (PL)

in early spectra the presence of strong, narrow Balmer emission lines on top of broad emission lines. Examples of prominent SNe IIn include 1978K (Ryder et al. 1993), SNe 1983K (Niemela, Ruiz & Phillips 1985), 1984E (Dopita et al. 1984), 1986J (Rupen et al. 1987; Leibundgut 1991), 1987F (Filippenko 1989; Wegner & Swanson 1994), 1988Z (Filippenko 1991; Stathakis & Sadler 1991; Turatto et al. 1993; Benetti et al. 1998), 1994W (Cumming, Lundqvist & Meikle 1994; Meikle et al. 1994; Sollerman, Cumming & Lundqvist 1998, hereafter SCL98), 1995G (Pastorello et al. 2002) and 1995N (Fransson et al. 2002). More recent examples of SNe II with narrow lines are SNe 1997cy (Germany et al. 1994; Turatto et al. 2000), 1998S (Filippenko & Moran 1998; Bowen et al. 2000; Leonard et al. 2000; Fassia et al. 2001; Chugai et al. 2002; Fransson et al. 2004), 1999E (Filippenko 2000; Rigon et al. 2003) and, most remarkably, SN 2002ic, which has been identified as a likely SN Ia in a dense circumstellar (CS) envelope (Hamuy et al. 2003), are more recent examples of SNe with narrow lines.

The general wisdom is that the narrow lines of SNe IIn originate from the ionized, dense circumstellar gas (Henry & Branch 1987; Filippenko 1991). The interaction of SN ejecta with the dense CS gas modifies the SN optical spectrum and may fully power the SN IIn luminosity (Chugai 1990, 1992). Interaction with the dense CS gas is indicated also by strong radio and X-ray flux detected in some SNe IIn. SNe IIn are diverse (Filippenko 1997), probably reflecting variations in CS gas density and structure (smooth vs. clumpy) and SN ejecta parameters (mass and energy). On top of this there is also the possibility of asymmetry of both the ejecta and CS gas. Nevertheless, the primary factors responsible for the diversity (mass of main-sequence star, explosion mechanism, structure of pre-supernova, mass-loss mechanism and history, and progenitor binarity) are still unknown. All these uncertainties, along with the possibility of using them to probe pre-supernova behaviour prior to core collapse, add to the interest in these phenomena.

SN 1994W, discovered on 1994 July 29 (UT dates are used throughout this paper) at the pre-maximum phase (Cortini & Villi 1994), is among the brightest known SNe IIn. Its proximity (25 ± 4 Mpc; SCL98) and early discovery made it an ideal case for detailed study. Preliminary interpretation of the spectra showed that SN 1994W exploded in the dense CS envelope with a characteristic radius of $\sim 10^{15}$ cm, while the amount of ejected ^{56}Ni was low ($< 0.015 M_{\odot}$; SCL98).

Here we further advance our understanding of both the CS envelope properties and the phenomenon of SN 1994W as a whole by analysing the spectra and photometry discussed by SCL98 as well as other, hitherto unpublished, spectra. In our study we take two different approaches to modelling the data. The first is the simulation of the $\text{H}\alpha$ profile, which provides an efficient and straightforward probe of the Thomson optical depth and density of the CS envelope. The second approach is a hydrodynamical simulation of the SN explosion and the light curve based upon the upgraded version of the code STELLA (Blinnikov et al. 1998, 2000). An early version of this code proved effective in computing the hydrodynamics and light curve for interaction with a dense CS envelope in the case of SN 1979C (Blinnikov & Bartunov 1993).

This paper has the following structure. We start with a description of the data (Sections 2 and 3) and the general picture which arises from a qualitative analysis (Section 4). Next we quantify parameters of the CS envelope using a thin-shell deceleration model and a line-profile simulation (Section 5). We then use the gross parameters of the recovered density distribution as input for detailed hydrodynamical modelling (Section 6). Our findings are summarized and discussed in Section 7.

2 OBSERVATIONS

2.1 Photometry

The photometric data were compiled and described in SCL98. In our light-curve models in Section 3 we use the photometry up to day 197, assuming SN 1994W exploded on 1994 July 14.0 (SCL98). For a discussion of the explosion date, see Section 3.

2.2 Spectroscopy

The spectroscopic observations are described in Table 1. Some of these, taken from La Palma, were presented in Table 2 of SCL98. We supplement them with spectra taken at the Lick, Keck, and Bologna Observatories. The data cover epochs 18–203 days after explosion. We now describe these spectra in detail.

The La Palma spectra were reduced using the FIGARO (Shortridge 1990) and NOAO IRAF¹ packages. The CCD frames were bias-subtracted, flat-fielded, and corrected for distortion and cosmic rays. Wavelength calibration was carried out using arc spectra of copper-neon and copper-argon lamps, and should be accurate to better than 0.1 \AA for the high-resolution WHT and INT spectra, 0.5 \AA for the low-resolution WHT and INT spectra, and 1 \AA for the NOT spectrum.

The Bologna spectrum was obtained with the Bologna Astronomical Observatory 1.5-m telescope with the spectrograph BFOSC on 1994 July 31.9 and reported by Bragaglia et al. (1994).

Spectra were also obtained at the Shane 3 m reflector at Lick Observatory on days 21, 49, 57, 79 and 89, and at the W. M. Keck II 10 m telescope on day 197. The Lick observations were made with the Kast double spectrograph (Miller & Stone 1993). The Keck spectrum was obtained using the Low Resolution Imaging Spectrometer (LRIS; Oke et al. 1993) with a $1200 \text{ lines mm}^{-1}$ grating. For details, see Table 1.

For the Lick data, all one-dimensional sky-subtracted spectra were extracted in the usual manner, and each spectrum was then wavelength and flux calibrated, as well as corrected for continuum atmospheric extinction and telluric absorption bands (Wade & Horne 1988; Bessell 1999; Matheson et al. 2000).

¹ IRAF (Image Reduction and Analysis Facility) is distributed by the National Optical Astronomy Observatories, which are operated by the Association of Universities for Research in Astronomy, Inc., under cooperative agreement with the US National Science Foundation.

Table 1. Log of spectroscopic observations

Date (UT)	Phase ^(a)	Telescope/ spectrograph	Spectral res. (Å)	Flux standard	Seeing (arcsec)	Wavelength coverage (Å)	Observers
1994 07 31.9	17.9	BAO/BFOSC	13	BD+25°3941	1.6	4600–7800	AB
1994 07 31.9	17.9	INT/IDS	0.25	—	2.6–3.0	6507–6675	EZ
1994 08 04	21.5	Lick/Kast	7	BD+17°4708	2.5	4250–7020	AJB, AF, CP
1994 08 13.9	30.9	WHT/ISIS	2.7	SP1337+705	1.1–1.7	4290–8005	MB
1994 09 01	49.5	Lick/Kast	5	BD+28°4211, BD+26°2606	4+	3120–10400	AJB, AF, TM
1994 09 08.9	56.9	WHT/ISIS	11	Grw+70°5824	0.9–2.9	3300–9360	RR
1994 09 08.9	56.9	WHT/ISIS	2.7	Grw+70°5824	1.0–1.5	4255–5060, 6345–7150	RR
1994 09 09	57.5	Lick/Kast	4	BD+28°4211, BD+26°2606, BD+17°4711	3–5	3140–9920	AJB, AF, TM
1994 10 01	79.5	Lick/Kast	4	Feige 110, BD+26°2606	2–3	3130–8040	AF, LH, TM
1994 10 11	89.5	Lick/Kast	4	Feige 110, BD+26°2606	3–4	3160–8020	AF, TM
1994 11 12.3	121.3	INT/IDS	6	—	1.6	5485–7370	RR, NO
1995 01 26.6	196.6	Keck/LRIS	6	HD 19445	1.2	5628–6939	AF, LH
1995 02 01.9	202.9	NOT/LDS	12	Feige 34	0.9	5000–10000	JS, RC

Note: (a) Days after 1994 July 14.0. (b) Observers: AB – A. Bragaglia; AF – A. Filippenko; AJB – A. J. Barth; CP – C. Peng; EZ – E. Zuiderwijk; JS – J. Sollerman; LH – L. Ho; MB – M. Breare; NO – N. O’Mahony; TM – T. Matheson; RC – R. Cumming; RR – R. Ruten.

The spectra were flux-calibrated by comparison with the standard stars listed in Table 1. The sky position of SN 1994W in late 1994 meant that the observations were made when the supernova was at rather low altitude, and correspondingly high airmass. We corrected for the difference in atmospheric extinction brought about by the differing zenith distances of the supernova and the standard star. Airmasses at different zenith distances were taken from the relation given by Murray (1983), and we used the tables of extinction coefficient versus wavelength for La Palma given by King (1985).

With two exceptions, all our spectra were taken at the parallactic angle (Filippenko 1982), minimising slit losses due to atmospheric dispersion. The first exception was the day 18 Bologna spectrum of SN 1994W, which shows considerable loss of flux in the blue. We corrected the slope of the spectrum to match the *B* and *V* photometry from the same night reported by Bragaglia et al. (1994) using filter functions from Gualandi & Merighi (2001).

The second exception was the standard-star observation for the day 31 La Palma spectrum. While the SN 1994W spectrum was taken at the parallactic angle, the standard-star spectrum was taken at an airmass of 1.6, with the slit at position angle 33° when the parallactic angle was 119°. No contemporary filter photometry is available for correcting the supernova spectrum. The effect on the day 31 supernova spectrum depends on how the standard star was positioned in the slit, which in turn depends on the combination of the spectral response of the acquisition camera at the telescope. The acquisition camera at the WHT in 1994 August was a Westinghouse ETV-1625 whose response curve peaked at 4400 Å, with half-power points at 3400 Å and 6200 Å (C. Jackman & D. Lennon, 2004, private communication). The standard star, Grw +70°5824, is a DA3 white dwarf with

a blue spectrum. It therefore seems likely that the slit was positioned so that maximum transmission was at around 4400 Å, at the blue end of the spectrum.

We have estimated the amount of flux that would be lost with wavelength, and find that the losses would largely have been at the red end of the standard spectrum — as much as 80 per cent of the flux at 8000 Å. The effect on the calibrated supernova spectrum was thus to make it appear redder than it really was. Since the day 31 spectrum is already remarkably blue (Section 3.1.3), we have made no further correction to the spectrum; the calibration can be regarded as a conservative estimate of the already extreme continuum slope.

No observations of flux standards were available for the INT spectra taken on days 18 and 121. A very rough flux-calibration of the day 18 INT spectrum was made by assuming that the flux in the wings of the H α line (at the red and blue edges of the spectrum) declined at the same rate as the visual magnitude estimates between days 18 and 31, i.e., by a factor of about 1.6 in f_λ . A similarly rough calibration of the day 121 spectrum was made by comparing with our *R*-band photometry from day 123 (SCL98).

The spectrum taken on day 197 was scaled so that the flux in the narrow H α feature matched that in the day 203 spectrum. The continua then match well in the overlap region.

Spectra from days 18, 57, 121 and 203 were displayed in SCL98 (their Figs. 2 and 3). They also showed the portion of the spectrum on day 31 covering H α .

As a final correction, we noted that all the spectra cover the entire *V* band, and we scaled each spectrum to match contemporary *V*-band photometry. The procedure was as follows. We assumed that the day 57 La Palma spectrum was correct. Next, we interpolated the *V* magnitudes in the light

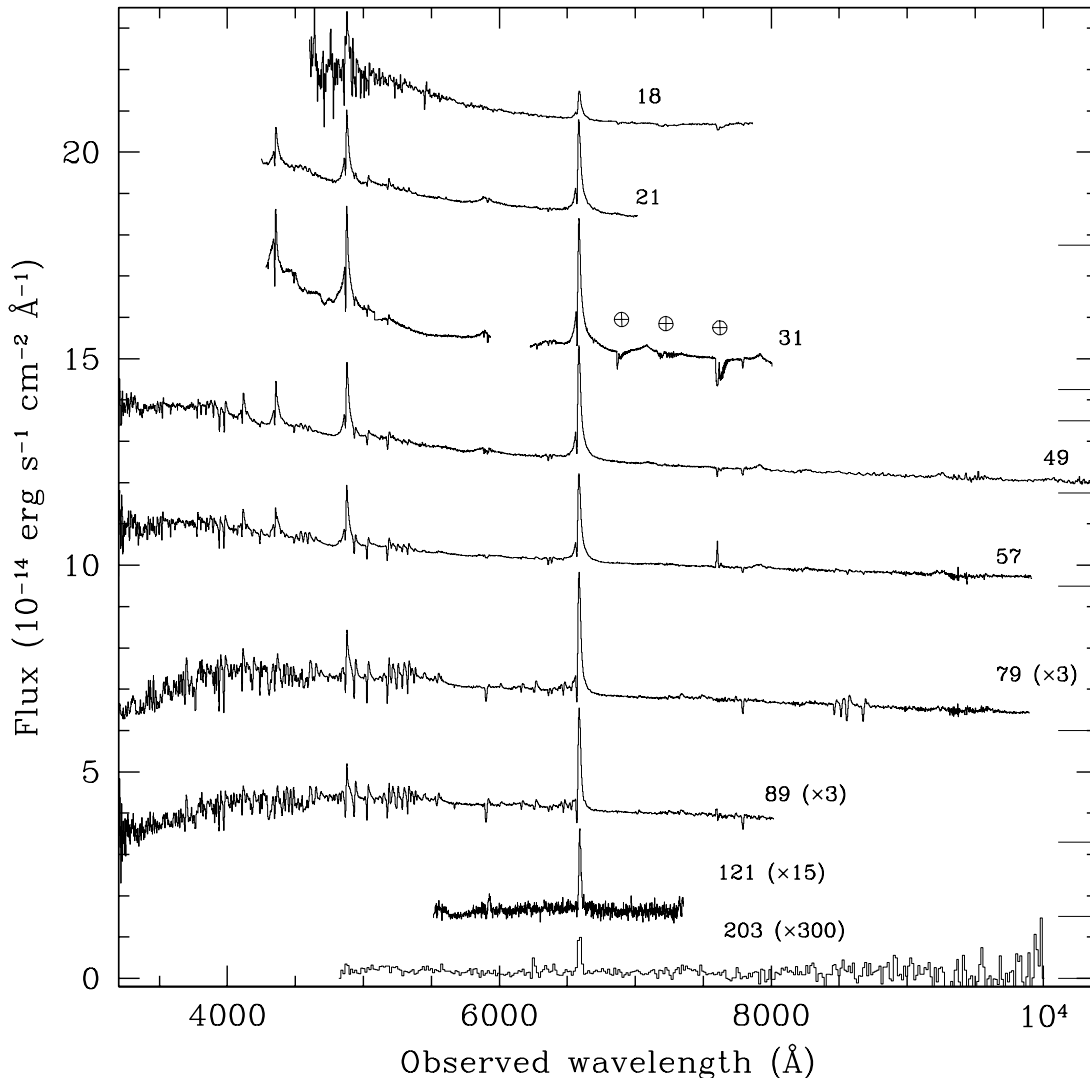


Figure 1. Spectra of SN 1994W: days 18–203. The spectra have been shifted vertically for clarity. No heliocentric correction has been applied to the wavelength scale. The ticks on the right-hand side mark the zero level for each spectrum. The spectra from day 79 and later have been multiplied by a constant, noted in parentheses. The La Palma spectra from days 18 and 57 and the day 197 Keck spectrum are not shown. Telluric absorption lines in the day 31 spectrum are marked.

curve presented by SCL98. This gave us relative fluxes in V for all the epochs. We then integrated all the plateau spectra (days 21–89), multiplying them by a standard V filter function (Allen 1973) with transmission values interpolated between points at 100-Å intervals. The whole spectrum was then scaled linearly in flux so that the integrated V magnitude corresponded to the V -band photometry in SCL98.

3 RESULTS

During the period of our observations, the spectrum of SN 1994W (Figs. 1 and 2) was dominated by narrow Balmer emission lines, initially with P-Cygni absorption features, and accompanied by a wide variety of weaker lines showing broad emission and/or narrow P-Cygni profiles (cf. Filippenko & Barth 1994). Line identifications are presented in Table 2 and in Fig. 3. In the following sections, we examine

the spectral development for each epoch in turn, and then concentrate on the individual features and ionic species.

In this section, quoted line fluxes (see Table 3) were measured by interpolating the neighbouring continuum across the line in question. The line fluxes are net fluxes and do not correct for the narrow P-Cygni absorption components.

3.1 Spectral evolution

3.1.1 Day 18

The low-resolution Bologna spectrum showed a blue continuum with prominent lines of $H\alpha$ and $H\beta$, which are narrow with broad wings. The latter have been interpreted as an effect of multiple Thomson scattering of line photons in the CS envelope (Chugai 2001). Our high-resolution spectrum for this epoch (Fig. 3 in SCL98) covers only the $H\alpha$ line, but shows a narrow P-Cygni absorption at about -800

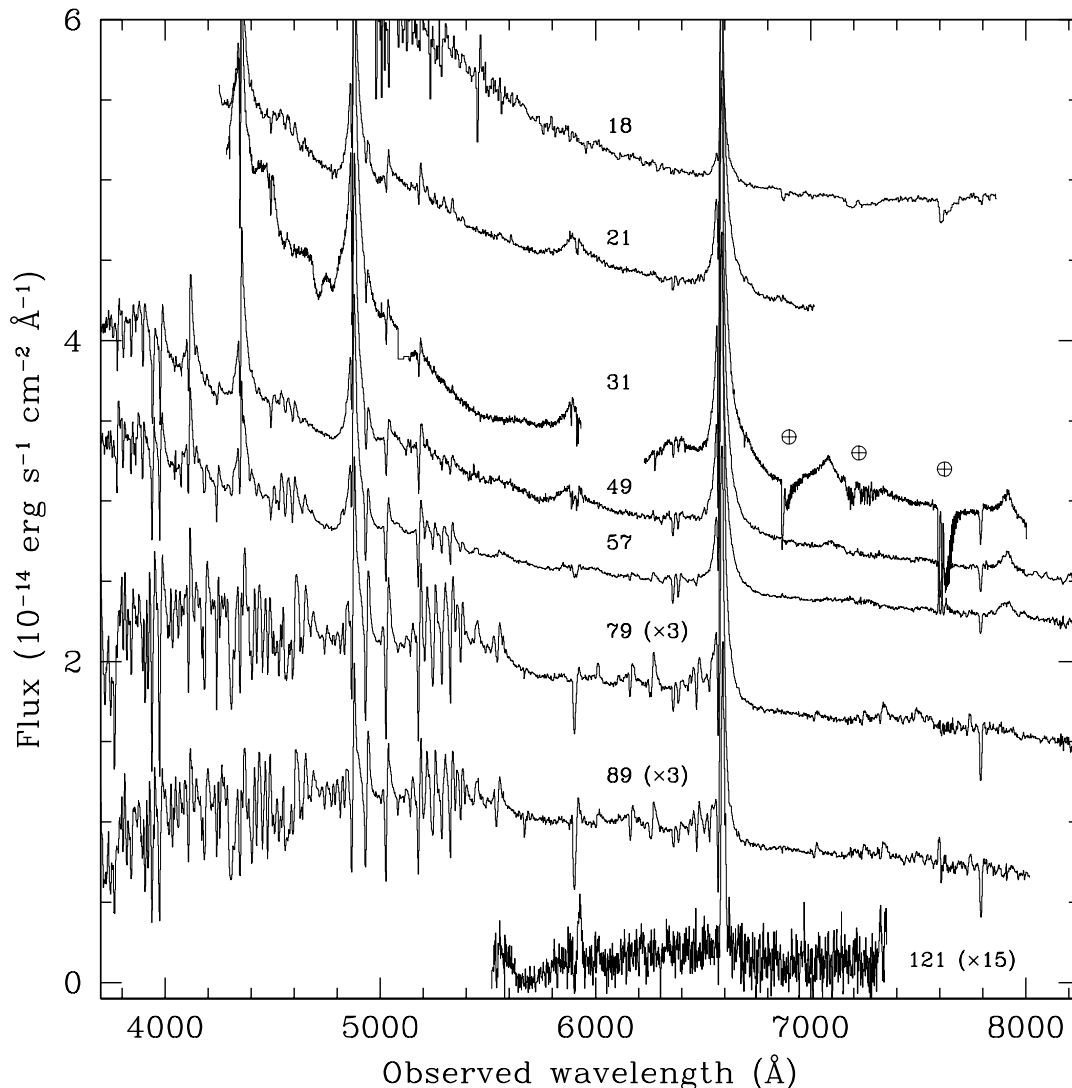


Figure 2. Spectra of SN 1994W: days 18–121. Same as Fig. 1, but with the ordinate stretched to show the weaker features more clearly. The day 197 and 203 spectra are omitted. Telluric absorption lines in the day 31 spectrum are marked.

km s^{-1} not visible in the low-resolution spectrum. The emission peak is close to the velocity of nearby H II emission, measured at $1249 \pm 3 \text{ km s}^{-1}$, which we adopt as our best estimate of the heliocentric velocity of the supernova. The interstellar Na I D lines give a somewhat lower value, $1185 \pm 15 \text{ km s}^{-1}$, measured from the day 31 spectrum.

3.1.2 Day 21

The rapid brightening of the supernova at this epoch (SCL98) was reflected in increasingly strong Balmer lines. The spectrum showed a strong blue continuum, and prominent lines of H α , H β and H γ , all exhibiting narrow P-Cygni profiles with broad emission wings. The Balmer decrement was remarkably shallow, with flux ratio H α :H β :H γ = 1.1:1:0.5 (dereddened assuming $E_{B-V} = 0.17$ mag from SCL98 and the reddening law of Cardelli, Clayton & Mathis 1989). The Balmer lines were accompanied by an asymmetric triangular broad emission feature corresponding to He I

$\lambda 5876$, possibly blended with the Na I D doublet, and many narrow P-Cygni lines of Fe II.

3.1.3 Day 31

By day 31, the blue continuum appeared to have steepened. The calibration of the spectrum is uncertain, as noted in Section 2 above, but the evidence suggests that the spectrum really was as remarkably blue as it appears to be. The Balmer lines still show a flat decrement, as on day 21, with measured ratios 1.2:1:0.6. The blue wings in H β and H γ appear to be stronger relative to the red wings, compared to day 21 (Fig. 5, right-hand panel).

Broad, triangular He I emission lines with full-width at half-maximum velocity width (v_{FWHM}) around 2500 km s^{-1} were stronger than on day 21 (Figs. 2 and 5). He I $\lambda 5876$ was accompanied by strong He I $\lambda 7065$. Broad He I $\lambda 6678$ appeared to fill out the red wing of H α , and the triplet line at $\lambda 4471$ is present as broad emission which underlies neighbouring Fe II lines. All but He I $\lambda 7065$ also showed

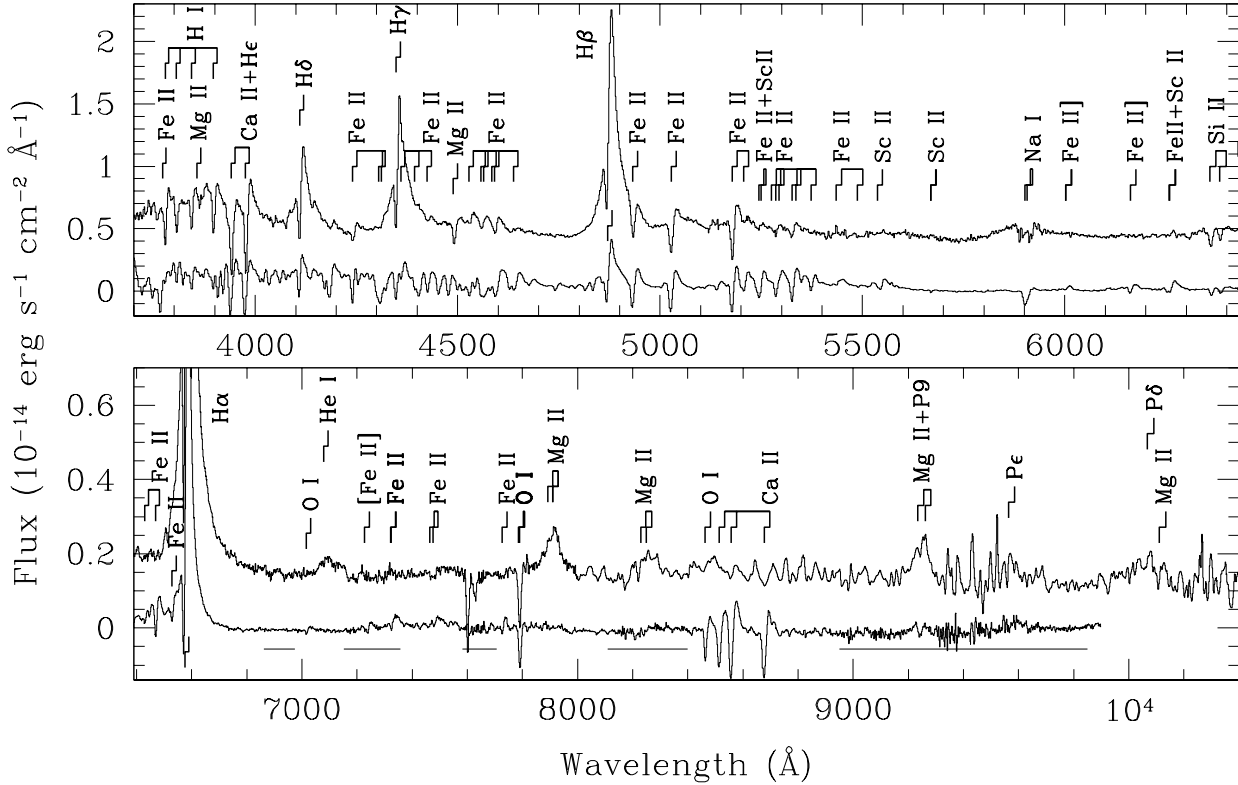


Figure 3. Line identifications for days 49 (upper spectrum) and 79. The spectra have been continuum-subtracted and shifted for clarity. Each line is indicated by a broken vertical bar marking heliocentric velocities -700 km s^{-1} and 0 km s^{-1} . Horizontal bars longward of 6700 Å mark regions where telluric absorption has been removed.

weak, narrow P-Cygni features with minima around -700 km s^{-1} .

A similarly triangular emission feature is seen at 7890 Å , which we identify with the Mg II triplet at $7877\text{--}7896 \text{ Å}$ (see Section 3.3.4).

Stronger narrow P-Cygni lines with absorptions around -600 km s^{-1} are seen in O I $\lambda 7773$, Si II $\lambda\lambda 6347, 6371$, and a large number of Fe II lines. The O I and Si II lines are dominated by absorption, while in Fe II the equivalent widths of the absorption and emission components are comparable.

3.1.4 Day 49

The day 49 spectrum (Figs. 1, 2 and 3) shows a redder continuum. The Balmer decrement steepened to 1.5:1:0.6. The He I $\lambda 5876$ and Na I D blend was again asymmetric as on day 21, and appeared to have a broader blue wing. The only other remaining He I line, $\lambda 7065$, is no longer as prominent as on day 31. The Mg II $\lambda 7877\text{--}7896$ feature was still clearly visible. Similar broad features were detected at $\sim 8230 \text{ Å}$ and $\sim 9220 \text{ Å}$, lending support to the identification with Mg II.

Many new Fe II lines are apparent, plus Ca II H & K and possibly the Ti II multiplet at around 3500 Å . The wider wavelength coverage picked up a large number of overlapping narrow P-Cygni lines in the blue; most of the identified ones are H I and Fe II.

3.1.5 Day 57

Eight days later, the Balmer decrement showed no significant change at 1.5:1:0.6. The spectrum showed ever stronger Fe II lines. No unambiguous trace of He I remained (Fig. 2), suggesting that the emission feature at $\sim 6000 \text{ Å}$ was now only due to Na I D. The emission in this feature broadened and flattened out, extending from -4000 km s^{-1} to $+6000 \text{ km s}^{-1}$ (Figs. 2 and 5). The Mg II $\lambda 7877\text{--}7896$ feature was still present, but appeared more flat-topped than on day 49. P-Cygni lines of O I $\lambda 8446$ and the Ca II near-infrared triplet, also weakly present on day 49, were clearly detected in the red.

3.1.6 Day 79

The continuum appeared again to have reddened (Fig. 1). The Balmer lines decreased in strength relative to the now very numerous Fe II P-Cygni lines (Figs. 2 and 3). The H α /H β ratio was now 2.7 ± 0.3 , close to Case B. Narrow overlapping absorption and P-Cygni features completely dominated in the blue. In the red, the feature at 7890 Å had disappeared, but O I $\lambda 8446$ and the Ca II triplet had increased in strength. The narrow absorption in Na I D had increased markedly in strength since day 57, and broad Na I emission was no longer apparent.

Narrow P-Cygni profiles of O I $\lambda 7002$ and Sc II appeared, the latter possibly accompanied by a broad emission

Table 2. Line identifications for days 18–121. Symbols are as follows: a — line seen in absorption only; b — broad emission, e — emission; p — P-Cygni profile; – (dash) — no feature detected, : (colon) — uncertain identification. The Fe II lines were identified with the help of the line lists of Fuhr, Martin & Wiese (1988) and Sigut & Pradhan (2003). Wavelengths in Å are from these references and from van Hoof (1999).

Identification	18	21	31	49	57	79	89	121	Identification	18	21	31	49	57	79	89	121
Fe II 3764.11									Sc II 5657.90								
+H11 3770.63				p	p	–	–		+Sc II 5658.36	–	–	–	–	–	a	a	
H10 3797.90				p	p	p	p		He I 5875.61	–	b	pb	b:	b:	–	–	–
H9 3835.38				p	p	p	p		Na I 5889.95								
Mg II 3849.3				p	p	–	–		+Na I 5895.92	–	b:	b:	ba:	ba:	p	p	ep:
H8 3889.05				p	p	p	p		Fe II] 5990.60								
Fe II 3914.51				–	–	p	p		+Fe II] 5991.38	–	–	–	–	–	ep	ep	–
Ca II 3933.66				p	p	p	p		Fe II] 6150.10	–	–	–	–	p	p	p	–
Ca II 3968.47									Sc II 6245.63								
+He 3970.07				pb	pb	pb	pb		+Fe II 6247.58	–	–	–	pb	pb	pb	pb	–
Hδ 4101.73				pb	pb	pb	pb		Si II 6347.11	–	p	p	p	p	p	p	–
Fe II 4233.12	–	–	–	p	p	p	p		Si II 6371.37	–	p	p	p	p	p	p	–
Fe II 4296.57									Fe II 6416.91	–	–	–	–	p	p	p	–
+Fe II 4303.17	–	–	–	–	p	p	p		Fe II 6456.38	–	–	–	–	p	p	p	–
Hγ 4340.46	–	pb	pb	pb	pb	pb	pb		Fe II 6517.02	–	–	–	–	p	p	p	–
Fe II 4351.76	–	–	–	–	p	p	p		Hα 6562.80	pb	pb	pb	pb	pb	pb	pb	e
Fe II 4385.38	–	–	–	p	p	–	–		He I 6678.15	–	p:	pb	–	–	–	–	–
Fe II 4416.83	–	–	–	p	p	p	p		O I 7002.20	–	–	–	–	–	p	p	–
He I 4471.5	–	–	ba	–	–	–	–		He I 7065.22	–		b	b	–	–	–	–
Mg II 4481.2	–	p	p	p	p	–	–		[Fe II] 7214.71	–	–	–	–	–	p	p	–
Fe II 4520.21	–	–	–	p	p	–	–		Ca II] 7291.47	–	–	–	–	–	–	–	e
Fe II 4549.46									Fe II 7308.07								
+Fe II 4555.88	–	p	p	p	p	p	p		+Fe II 7310.22	–		–	–	–	p	p	–
Fe II 4576.34									Ca II] 7323.89	–		–	–	–	–	–	e
+Fe II 4582.83	–	p	p	p	p	p	p		Fe II 7449.34	–		–	–	–	p	p	
Fe II 4629.34	–	p	–	p	p	p	p		Fe II 7462.41	–		–	–	–	p	p	
Hβ 4861.32	pb	pb	pb	pb	pb	pb	pb		Fe II 7711.72			–	p	p	p	p	
Fe II 4923.94	p:	pb	pb	pb	pb	pb	pb		O I 7773.8	p		p	p	p	p	p	
Fe II 5018.44	p:	pb	pb	pb	pb	pb	pb		Mg II 7877-96			b	b	b	–	–	
Fe II 5169.05	–	p	p	p	p	p	p		Mg II 8213.98								
Fe II 5197.59	–	p		p	p	p	p		+Mg II 8234.64				b:	b:			
Fe II 5234.63									O I 8446.36				p	p	p		
+Sc II 5239.81	–	–	–	–	p	p	p		Ca II 8498.03				–	–	p		
Fe II 5264-84	–	p	–	p	p	p	p		Ca II 8542.09				p	p	p		
Fe II 5316.62									Ca II 8662.14				–	p	p		
+Fe II 5325.54	–	p	p	p	p	p	p		Mg II 9218.25								
Fe II 5362.85	–	–	–	–	p	p	p		+Pa9 9229.01								
Fe II 5425.26	–	–	–	–	pe	pe	pe		+Mg II 9244.26				b	b	b		
Fe II 5477.66	–	–	–	–	–	p	p		Paε 9545.97				pb:	pb:	pb:		
Sc II 5526.79	–	–	–	–	pb	pb	pb	p:	Paδ 10049.4								
									+Mg II 10092.1				b:				

component. Semi-forbidden lines of Fe II] $\lambda\lambda 5991, 6150$ were clearly detected for the first time.

3.1.7 Day 89

The spectrum on day 89 was essentially the same as on day 79, but was weaker and showed a redder continuum. The H α /H β ratio increased to 5.2 ± 1.3 , and H γ was now blended with Fe II lines. Both Na I D and O I $\lambda 7002$ continued to increase in strength.

3.1.8 Day 121

Our spectrum for day 121 (Figs. 1 and 2) has smaller wavelength coverage and rather poor signal-to-noise ratio, but it

is obvious that a dramatic change had occurred since day 89, paralleling the supernova's precipitous fading after day ~ 110 (SCL98).

As reported by SCL98, three narrow emission lines are unambiguously detected: H α with a v_{FWHM} of 780 km s^{-1} , plus much fainter Na I D ($v_{\text{FWHM}} = 775 \text{ km s}^{-1}$) with a P-Cygni absorption component, and Ca II] $\lambda 7291$ ($v_{\text{FWHM}} = 475 \text{ km s}^{-1}$) close to the red edge of the spectrum. The emission peak of H α had moved farther to the red than on day 89, at about $+70 \pm 100 \text{ km s}^{-1}$. The Sc II P-Cygni feature at 5530 Å appears also to have survived since day 89, showing a sharp absorption feature at $-800 \pm 100 \text{ km s}^{-1}$.

Underlying the narrow features is what appears to be a low, undulating continuum. SCL98 argued that the sharp drop to zero flux at 5620 Å was evidence that the contin-

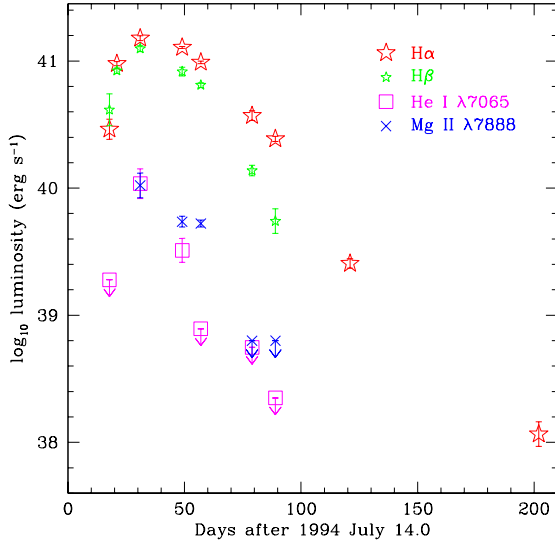


Figure 4. Luminosity evolution of various lines. Line fluxes are detailed in Table 3. A distance of 25.4 Mpc and an extinction of $E_{B-V} = 0.17$ mag were adopted.

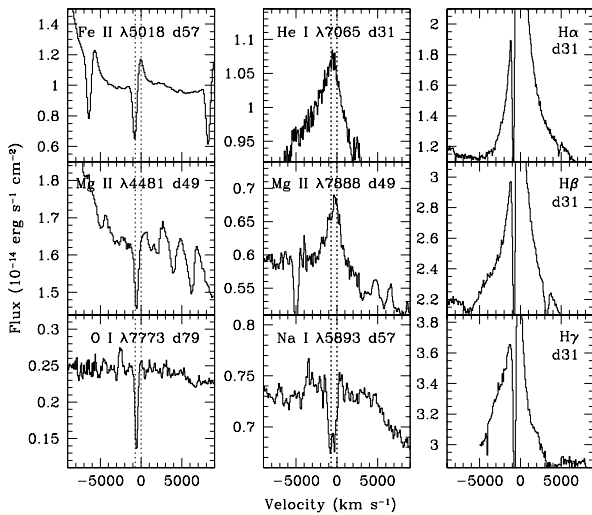


Figure 5. Selected line profiles; day numbers are indicated. The left-hand panel shows examples of narrow P-Cygni profiles, the middle panel shows broad lines (note the extended wings in Na I on day 57), and the right-hand panel shows the wings of the H I lines on day 31. The dotted vertical lines mark velocities of 0 and -700 km s^{-1} .

uum was rather composed of broad, overlapping emission lines. The steepness of the drop at 5620 \AA indicates that the velocity widths of such lines can be no greater than $\sim 5000 \text{ km s}^{-1}$. Similar features have been seen in late-time spectra of the SN IIn 1997cy (Germany et al. 1994; Turatto et al. 2000). A sharp drop at this wavelength is in fact also typical of SNe Ia and some SNe Ib/Ic at late times, when the emission is dominated by lines of Fe II and [Fe II] (see

Axelrod 1980). These similarities suggest that SN 1994W had reached its nebular phase at this epoch.

3.1.9 Day 197

Our spectrum, not shown in Figs. 1 and 2, detected only H α , which was perhaps just resolved. Its velocity width was $v_{\text{FWHM}} \approx 625 \text{ km s}^{-1}$, consistent with no change since day 121. Na I emission at the same strength relative to H α as on day 121 would not have been detected, given the low signal-to-noise ratio of the spectrum.

3.1.10 Day 203

The day 203 spectrum (Fig. 1) confirms that narrow, unresolved H α is the only detectable feature from the supernova. The galaxy background probably dominates the remaining, noisy continuum, though photometry indicates that the supernova can account for up to 50 per cent of the flux (SCL98). SCL98 put limits on the flux in broad lines of width $\sim 4500 \text{ km s}^{-1}$.

3.2 General spectral appearance

3.2.1 Line profiles

The spectra reveal two major types of line profile-forming components (SCL98; Fig. 5): narrow P Cygni profiles and broad lines. However, careful inspection reveals that while the blue velocity at zero intensity (BVZI) of the broad lines does not exceed -5000 km s^{-1} , H α at the luminous stage shows a red wing extending at least up to $+7000 \text{ km s}^{-1}$. This wing is clearly detectable in H α on days 31, 49 and 57 (Figs. 2 and 5). We believe that this wing is caused by a Thomson scattering effect in the expanding CS envelope (see also Section 4). Since the intensity of the Thomson scattering wing is proportional to the line intensity, the wing may be present but not obvious in other, weaker lines.

The intrinsically broad lines typically have a triangular profile. On day 31 they show an apparent skewing toward the blue, possibly due to an occultation effect. The Na I doublet on day 57 shows a flat-topped profile with $\text{BVZI} \approx 4000 \text{ km s}^{-1}$. No other line shows such a flat-topped profile, nor does Na I doublet at other epochs, though the feature is dominated by He I $\lambda 5876$ earlier than this. This suggests that the material emitting Na I has a narrower distribution of velocity than the other broad lines (see Section 4.2).

3.2.2 Line strengths

Assuming a distance of 25.4 Mpc to NGC 4041 and $E_{B-V} = 0.17$ mag (SCL98), we have plotted the luminosity evolution of the strongest emission lines in Fig. 4. Note the quasi-exponential decline of the H α luminosity with exponential lifetime ~ 21 days. This fast decline is in dramatic contrast to other SNe IIn, for example SN 1995G, whose narrow H α luminosity dropped by only a factor of three during the first 600 days (Pastorello et al. 2002). The fast decay of the H α luminosity is consistent with a small amount of ^{56}Ni in SN 1994W (SCL98) and also indicates the absence of dense CS gas at large distances from the pre-supernova (see Section 7).

Table 3. Flux measurements of emission lines, in units of 10^{-14} erg s $^{-1}$ cm $^{-2}$.

Line	Day								
	18	21	31	49	57	79	89	121	203
H γ 4340.46	—	30(2)	47(4)	34(1.5)	24.5(2)	—	—	—	—
H β 4861.32	30(10)	61(3)	91(5)	60(5)	47(2)	10(1)	4(1)	—	—
Fe II 5018.44	—	1.7(0.1)	0.7(0.1)	2.1(0.5)	2.7(0.7)	2.0(0.7)	1.6(0.2)	—	—
He I 5875.62	—	—	—	—	—	—	—	—	—
+Na I ^(a) 5889-95	—	13.6(2)	14(4)	12(1)	5(1)	<1	<1	—	—
Na I ^(b) 5889-95	—	—	—	—	0.14(0.05)	0.2(0.02)	0.6(0.1)	0.11(0.03)	<0.03
H α 6562.80	25(5)	82(3)	130(6)	110(2)	84(2)	32(3)	21(1)	2.2(0.2)	0.1(0.025)
He I 7065.22	<2	—	9.7(3)	2.9(0.7)	<0.7	<0.5	<0.2	—	—
Mg II ^(a) 7877-7896	—	—	10(2.5)	5.2(0.5)	5.0(0.3)	<0.6	<0.6	—	—
Mg II 9218-44	—	—	—	—	6.3(1)	7.5(0.8)	1.0(0.3)	—	—

Notes: (a) blend, (b) emission component only.
Error estimates are 1σ . Upper limits are 3σ .

3.2.3 Continuum

We carried out black-body fits to the continuum. We obtain colour temperatures of 13000 ± 2000 K on day 21, 15000 K on day 31, 10000 K on days 49 and 57, 7200 K on day 79 and 7200 K on day 89. We find that the black-body fits work best for $E_{B-V} = 0.15$ mag, consistent with our estimate from Na I absorption (0.17 ± 0.06 mag; SCL98).

3.3 Elements identified

3.3.1 Hydrogen

We detect the Balmer series from H α to at least H11, and possibly also members of the Paschen series from Pa δ to Pa11 (Fig. 3). The profiles seem to be a combination of broad emission line with BVZI $\gtrsim 4000$ km s $^{-1}$ and a narrow P-Cygni absorption component (~ 1000 km s $^{-1}$). The ratio of narrow-to-broad emission component decreases from H α toward the higher Balmer lines. This indicates a nearly normal Balmer decrement for the narrow component and a flat or possibly inverse Balmer decrement for the broad component (Fig. 5).

A flat or inverted decrement suggests strong deviation from the recombination case, related to collisions and radiative transitions in the field of the photospheric radiation. The observed line ratios suggest an excitation temperature for hydrogen's excited levels of around 15000 K. Two different thermalization mechanisms for hydrogen levels may operate in this situation: the level populations may be controlled by radiative transitions in the field of the external black-body photospheric radiation, or thermalization may be primarily collisional. Both mechanisms have been exploited to account for flat or inverted Balmer decrements observed in cataclysmic variables (Elitzur et al. 1983; Williams & Shipman 1988). Both thermalization mechanisms are plausible in SN 1994W as well.

3.3.2 Helium

We observe broad He I lines with triangular emission profiles and narrow P-Cygni features. The He I lines disappear after day 49 (Figs. 2 and 4; Table 2). He I $\lambda 5876$ and $\lambda 7065$ appear

only in emission. He I $\lambda 4471$ and $\lambda 6678$ show weak absorption features. A high ratio $I(7065)/I(5876) \approx 0.5$ indicates a large contribution of collisional and/or radiative excitation compared to the purely recombination case. Unfortunately, this fact cannot be used as a straightforward indicator of electron concentration in the line-emitting region. Computations for an extended parameter set (Almog & Netzer 1989) show that this particular ratio may be reached in a wide range of concentrations ($n_e \approx 10^4 - 10^{14}$ cm $^{-3}$), with pronounced dependence on the optical depth in He I $\lambda 3889$.

3.3.3 Oxygen

O I $\lambda 7773$ is present with an absorption-dominated P-Cygni profile from as early as day 18 to day 89. From day 79, we tentatively identify O I $\lambda 7002$ with a P-Cygni profile. This line has not to our knowledge been seen in a supernova spectrum before, but was identified in the proto-planetary nebula Henize 401 (García-Lario, Riera & Manchado 1999), whose low-ionization spectrum bears some similarity to that of SN 1994W at these phases.

3.3.4 Other metals

Ca II H & K were strong in absorption at all epochs when we covered them. The near-infrared triplet lines were weak on day 49, but strengthened dramatically by day 79 (Fig. 3). This may reflect an increase in the Ca II/Ca III ratio with the drop in radiation temperature at late epochs.

The Na I D doublet's development is remarkable (Figs. 1, 2 and 5), even taking into account blending with interstellar absorption and in the earlier spectra with He I $\lambda 5876$. Up to day 49, a flat-topped profile emerged as He I faded. From day 57 on, the strength of the circumstellar P-Cygni absorption increased, presumably as a result of increasing Na I ionization fraction.

Magnesium lines appear both in absorption and emission. Narrow absorption with weak P-Cygni emission is seen in Mg II $\lambda 4481$ from day 21 to day 57. We identify Mg II $\lambda 7877-7896$ as the source of the broad feature around 7890 Å. As an alternative interpretation, we considered [Fe XI] $\lambda 7892$. Strong [Fe XI] might be expected to be accompanied by emission in [Fe X] $\lambda 6374$, and there may

indeed be a broad feature underlying the Si II absorption lines to the blue of H α . However, this feature does not persist to later epochs as the 7890 Å feature does, nor are any other high-ionization lines identified at any epoch. In addition, emission lines with similar widths to the 7890 Å feature are seen at wavelengths corresponding to Mg II transitions around 9230 Å, and possibly at 8200 Å and 10900 Å. Nevertheless, we find it somewhat surprising that the broad emission in Mg II $\lambda\lambda 7877\text{--}7896$ is not accompanied by similar emission in O I $\lambda 7773$.

The doublet of Si II $\lambda\lambda 6347, 6371$ is present from days 21 to 89, showing absorption-dominated P-Cygni profiles. The lines weakened relative to other features on days 79 and 89. Si II $\lambda 6240$ therefore seems to be an unlikely contributor to the feature at 6260 Å (see below), which increases on these dates.

Sc II emission lines at around 5530 Å and 6250 Å were identified by Pastorello et al. (2002) in the spectrum of the Type IIn SN 1995G. We identify both Sc II $\lambda 5527$ and $\lambda 6246$ in our spectra, and Sc II may contribute to the feature at 6260 Å. In particular, $\lambda 5527$ shows some evidence of a broad emission component (Figs. 2 and 3). Its narrow P-Cygni core apparently persisted until day 121.

We identify a host of Fe II lines (Fig. 3; Table 2), all of which show narrow P-Cygni profiles. They may also be accompanied by broad emission as in the case of other species, since the spectra show hints of underlying broad emission in regions of the spectrum where there are many Fe II lines (Fig. 1). By days 79 and 89, a few lines of forbidden and semi-forbidden Fe II are identified. These have emission-dominated P-Cygni profiles (Fig. 3).

4 GENERAL PICTURE

The previous discussion of spectroscopic and photometric data on SN 1994W (SCL98) led to the conclusion that the narrow lines originate in a dense CS envelope. However, at present, the spectroscopic and photometric results cannot readily be incorporated into any existing model of a SN II interacting with a CS environment. We therefore present first our qualitative view of what we observe in the case of SN 1994W. We emphasize some basic elements of the physical picture that, in our opinion, are crucial for understanding the phenomenon.

4.1 The opaque cool dense shell

The smooth continuum of SN 1994W and its lack of broad absorption lines is typical of most SNe IIn at an early phase. It is also reminiscent of the early spectrum of SN 1998S (Leonard et al. 2000). For SN 1998S, the smooth continuum and the absence of broad absorption lines was explained as an effect of an opaque cool dense shell (CDS) which formed at the interface of the SN with its circumstellar medium (Chugai 2001). In this situation, an opaque CDS is physically equivalent to an expanding photosphere with a sharp boundary and without an external, extended SN atmosphere. In comparison, the CDS formed in supernova remnants during the radiative stage (Pikelner 1954) and in SNe interacting with a moderately dense CS wind

(Chevalier & Fransson 1985) are optically thin in the continuum.

The large optical depth of the CDS requires a relatively large swept-up mass. This may be a natural consequence of shock break-out in SNe II with extended stellar envelopes (Grasberg et al. 1971; Falk & Arnett 1977; Blinnikov & Bartunov 1993) and/or with extended CS envelopes of unusually high density. In the model of a pre-supernova with initial radius $\sim 10^{15}$ cm (Falk & Arnett 1977), a CDS with a mass of $\sim 2 M_{\odot}$ forms and remains opaque for about 70 days. We propose that a similar opaque CDS formed in SN 1994W. This suggestion finds support in the exceptionally bright peak of the light curve, $M_V \approx -19.5$ mag (SCL98, their Fig. 5). According to the theory of SN II light curves, a broad luminous maximum with $M \approx -(19\text{--}20)$ mag requires the explosion of a very extended pre-supernova with an envelope radius of $R_0 \approx 10^{15}$ cm (Grasberg et al. 1971; Falk & Arnett 1977).

4.2 The broad-line region

The deceleration of the CDS in the extended pre-supernova envelope and in the dense CS environment is accompanied by the Rayleigh-Taylor (RT) instability (Falk & Arnett 1977; Chevalier 1982). The growth and subsequent fragmentation of RT spikes in the dense CDS material results in the formation of a narrow layer ($\Delta R/R \approx 0.1\text{--}0.15$) composed of dense filaments, sheets and knots embedded in the rarefied hot gas behind the forward shock (Chevalier & Blondin 1995; Blondin & Ellison 2001). This mixed layer on top of the CDS is likely responsible for the broad emission lines observed in SN 1994W. If this is the case, then the expansion velocity of the CDS (v_s) should be the same as the velocity of the broad line-emitting gas, i.e., $v_s \approx 4000$ km s $^{-1}$.

A drawback of this picture of the broad-line formation is that the velocity distribution of the line-emitting gas peaks at the CDS expansion velocity v_s , which means the expected line profile should be boxy. With the exception of the Na I profile on day 57, the broad lines are instead triangular.

A triangular profile can be produced, however, if the spherically symmetric velocity distribution of the line-emitting matter is close to $dM/dv \propto v$. Actually, given this mass-velocity spectrum and constant emissivity per unit mass, and assuming that the velocity field is spherically symmetric, the luminosity distribution over the radial velocity u (in units of v_s) is

$$\frac{dL}{du} \propto \int_{|u|}^1 \frac{1}{v} \frac{dM}{dv} dv \propto (1 - |u|), \quad (1)$$

which is indeed triangular.

The broad velocity spectrum of the dense gas in the mixed layer may naturally arise in two plausible scenarios. In the first scenario the CS gas is clumpy. In this case, an ensemble of dense CS clouds engulfed by the forward post-shock gas could provide a broad velocity spectrum of radiative cloud shocks and cloud fragments (Chugai 1997) in the range of 1000–4000 km s $^{-1}$, where the lower limit is the CS velocity. This model may be characterized as low-velocity clouds in a high-velocity flow.

Alternatively, dense high-velocity clumps interacting with the low-velocity CS gas could produce a similar spec-

trum of fragments. This could occur if the forward shock is radiative, forming a thin post-shock layer with $\Delta R/R < 0.1$. In this situation, dense RT spikes, formed at the previous stage of RT instability of the CDS, can penetrate into the pre-shock zone. The interaction of these protrusions with the CS gas in the pre-shock zone leads to further fragmentation and deceleration of fragments down to the velocity of the CS gas. As a result, a broad velocity spectrum of dense cool fragments emerges in the velocity range of 1000–4000 km s⁻¹.

For this second possibility to hold, a high CS density n is needed to maintain the narrow width of the post-shock cooling region,

$$l_c = \frac{m_p v_s^3}{32n\Lambda}, \quad (2)$$

where m_p is the proton mass, and Λ is the cooling function in the post-shock zone. To reach the required ratio $l_c/R \approx 0.1$ at radius $R = 10^{15}$ cm, one needs a CS density of $n \approx 1.7 \times 10^9$ cm⁻³ assuming $\Lambda = 2 \times 10^{-23}$ erg s⁻¹ cm⁶ and $v_s = 4000$ km s⁻¹.

Both scenarios for the velocity spectrum leave open the question of why the velocity distribution of the line-emitting gas in the mixed layer is close to $dM/dv \propto v$. The following naive model seems to provide a hint.

Let us consider the interaction of a high-velocity fragment with the CS gas. In the rest frame of the initial fragment, the fragmentation process in the rarefied CS flow with the velocity $\approx v_s$ may be thought of as a stripping flow with accelerating velocity v_1 and in which the “radius” a of fragments progressively decreases as the velocity v_1 increases (Klein, McKee & Colella 1994). Assuming mass conservation of fragments in velocity space, $Q = dM/dt = (dM/dv)(dv/dt) = \text{constant}$, the mass-velocity spectrum of fragments may be expressed as

$$\frac{dM}{dv_1} = Q \left(\frac{dv_1}{dt} \right)^{-1}, \quad (3)$$

which is essentially determined by the acceleration dv_1/dt . The latter can be approximately described as acceleration due to the drag force

$$m \frac{dv_1}{dt} = \pi a^2 \rho (1 - v_1)^2, \quad (4)$$

where the velocity is in units of v_s , $m = (4\pi/3)a^3\rho_f$ is the mass of fragment of the density ρ_f , and ρ is the density in the rarefied ambient flow. To determine the acceleration we must specify the relation between fragment size and velocity $v = 1 - v_1$ relative to the CS gas. We assume that the fragment size for each new generation of cloudlets is tuned to the Kolmogorov turbulent cascade with spectrum $v \propto a^{1/3}$. With this relation, equation (4) leads to $dv_1/dt \propto 1/v$. The latter combined with equation (3) leads to a mass-velocity spectrum $dM/dv \propto v$.

A similar analysis carried out for the case of a CS cloud in the SN flow produces a quite different mass-velocity spectrum, $dM/dv \propto (1-v)$. This spectrum also results in a broad line but with zero slope at $|u| = 1$ and a narrow logarithmic peak: $dL/du \propto (|u| - 1 - \ln |u|)$. While this profile resembles the observed H α profile, it is at odds with the triangular profile of He I lines. Below (Section 5.4) we argue against a large contribution of CS clouds in the formation of H α .

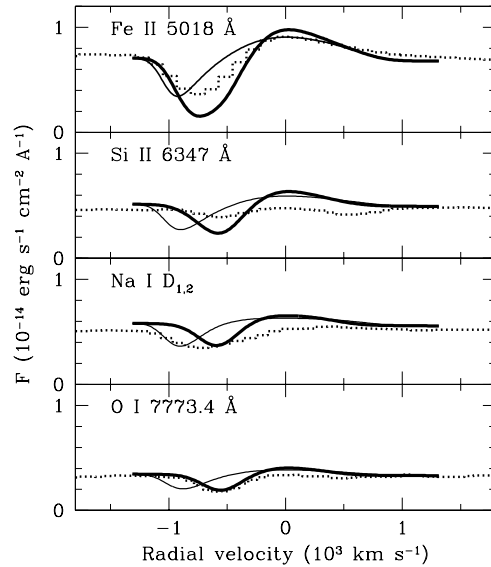


Figure 6. Circumstellar lines on day 79. Overplotted on the observational data (dotted line) are the models for homologous expansion (thick line) and the constant-velocity case (thin line).

4.3 The circumstellar envelope

4.3.1 Expansion kinematics

The radial velocities of narrow absorption features in SN 1994W are strikingly persistent between days 18 and 89. This implies that the expansion velocity of the CS envelope (~ 1000 km s⁻¹) has a pre-explosion origin. An alternative possibility — acceleration of a slow wind by SN radiation (see also SCL98) — seems unlikely, since it would require unrealistic fine tuning between the time-dependent luminosity and absorption (scattering) coefficient to arrange the persistence of the velocity of accelerated gas.

Two extreme options are conceivable for the CS envelope’s pre-explosion kinematics: constant-velocity flow and homologous expansion ($u \propto r$). The former might be the result of either continuous wind outflow or a succession of ejection events with similar ejecta velocities. Homologous expansion, on the other hand, might be produced by a single explosive ejection. The latter mechanism, though exotic, was in fact proposed by Grasberg & Nadyozhin (1986) to account for the narrow CS lines in SN 1983K.

4.3.2 Envelope size

The light curve of SN 1994W is characterized by a broad maximum around day 30 and a subsequent plateau, terminated by a sudden drop in luminosity at $t_d \approx 110$ d (SCL98, their Fig. 5). Assuming a CDS expansion velocity of $v_s = 4000$ km s⁻¹, we find that during this period the CDS sweeps up the CS gas within the radius $R_d = v_s t_d \approx 4 \times 10^{15}$ cm. Although this estimate refers to $t = 110$ d, we adopt it as a rough estimate for earlier epochs as well.

We now argue that this radius should coincide with the outer radius of the dense CS envelope, $R_{cs} \approx R_d$. If instead $R_{cs} > R_d$, then the light curve of SN 1994W should not have shown such a steep drop, since the CS interaction

would have augmented the luminosity at the luminosity decay phase. Equally, if $R_{\text{cs}} < R_{\text{d}}$, the narrow lines would have disappeared at epoch $t < t_{\text{d}}$, which was not observed. These arguments, therefore, provide strong evidence that the extent of the dense CS envelope is $R_{\text{cs}} \approx R_{\text{d}} \approx 4 \times 10^{15}$ cm. Beyond this radius, the CS density presumably drops steeply, as indicated both by the broad-band light drop after day 100 and the fast decline of the $\text{H}\alpha$ luminosity (Fig. 4). At larger radii, X-ray observations suggest that other density enhancements may be present (Section 7; Schlegel 1999).

4.3.3 Electron-scattering wings and circumstellar density

We attribute the extended smooth wings observed in $\text{H}\alpha$ and $\text{H}\beta$ between days 18 and 89 to the effect of Thomson scattering on thermal electrons participating in the bulk expansion of the CS envelope (Chugai 2001). Based on previous computations of Thomson scattering effects in SN 1998S, and the strength of the $\text{H}\alpha$ wings in SN 1994W on day 57 (when blending with $\text{He I } \lambda 6678$ was negligible), we believe that the optical depth of the CS envelope to Thomson scattering (τ_{T}) at this stage must have been close to unity.

Adopting a photospheric radius $R_{\text{p}} \approx v_{\text{s}} t = 2 \times 10^{15}$ cm on day 57 (where $v_{\text{s}} \approx 4000$ km s $^{-1}$) and an outer radius of the CS envelope $R_{\text{cs}} = 4 \times 10^{15}$ cm, we obtain an estimate of the average electron concentration in the CS envelope assuming $\tau_{\text{T}} \approx 1$:

$$n_{\text{e}} \approx \frac{\tau_{\text{T}}}{\sigma_{\text{T}}(R_{\text{cs}} - R_{\text{p}})} \approx 10^9 \text{ cm}^{-3}. \quad (5)$$

This value, taken together with the forward shock-wave velocity ($v_{\text{sh}} \approx 3000$ km s $^{-1}$), after correction for the CS velocity, provides an estimate of the density of the CDS material in the broad-line region (n_{cds}). The pressure equilibrium condition, with sound speed in the CDS matter of $c_{\text{s}} \approx 15$ km s $^{-1}$, results in $n_{\text{cds}} \approx n(v_{\text{sh}}/c_{\text{s}})^2 \approx 4 \times 10^{13}$ cm $^{-3}$. This tremendous density provides a natural reason for the strong collisional thermalization of the broad component indicated by the observed inverse Balmer decrement (Section 3.3.1).

4.3.4 Circumstellar density from narrow lines

The strength of narrow subordinate lines indicates a high density in the CS envelope, as noted by SCL98. The simplest density estimate may be taken from the condition that the optical depth in a line of Fe II, for example $\lambda 5018$, is on the order of unity. This follows from the relative intensity of the absorption component of this line (~ 0.5). Assuming that level populations of Fe II obey the Boltzmann distribution for $T = 10^4$ K, one obtains for solar Fe/H a hydrogen concentration of $n \approx 3 \times 10^7 v_8 r_{15}^{-1} f_2^{-1}$ cm $^{-3}$. Here r_{15} is the linear scale of the line-forming zone in units of 10^{15} cm, v_8 is the velocity dispersion in units of 10^8 km s $^{-1}$, and f_2 is the ionization fraction of Fe II. Given the scale of the CS envelope ($\sim 4 \times 10^{15}$ cm), we thus have a lower limit $n > 10^7$ cm $^{-3}$. This lower limit should be considered as a revised version of the estimate reported in SCL98.

A somewhat more elaborate estimate of the density may be obtained using several different lines and assuming a quasi-local thermodynamic equilibrium (quasi-LTE) approximation, i.e., the Saha-Boltzmann equations corrected

for both geometrical dilution W and dilution of the photospheric brightness ξ . The latter defines the photospheric brightness through the black-body brightness $I_{\nu} = \xi B_{\nu}(T)$. We adopt a simple density distribution in the CS envelope: a plateau with a steep outer drop

$$n = n_0 / [1 + (r/R_{\text{k}})^{12}], \quad (6)$$

where the cutoff radius $R_{\text{k}} \approx R_{\text{cs}} = 4 \times 10^{15}$ cm. We consider two cases for the CS kinematics: free expansion ($v = hr$), with outer velocity at $r = 6 \times 10^{15}$ cm equal to $v_{\text{b}} = 1100$ km s $^{-1}$, and constant-velocity flow with $v = 1100$ km s $^{-1}$. The photospheric radius on day 79 is estimated as $R_{\text{p}} \approx v_{\text{s}} t \approx 2.7 \times 10^{15}$ cm, where $v_{\text{s}} = 4000$ km s $^{-1}$, while the temperature is taken to be $T_{\text{p}} = 7200$ K according to the value found from the black-body fit to the continuum (Section 3.2.3). The parameter ξ in this case is found to be 0.26.

In Fig. 6 we show calculated profiles of Fe II $\lambda 5018$, Si II $\lambda 6148$, the Na I D $_{1,2}$ doublet and the O I 7773 Å triplet, for solar abundance and hydrogen concentration $n_0 = 1.5 \times 10^9$ cm $^{-3}$. In the case of Na I we have for the sake of simplicity ignored the doublet structure, which explains why our model line is narrower than the observed one. This density seems to be the optimal one: a factor of 1.5 lower density results in too weak O I and Na I lines, while a factor 1.5 higher density makes all the lines too strong.

Although neither kinematic model produces an excellent fit, it is clear that free expansion kinematics better predicts the positions of the absorption minima and, therefore, is preferred compared to the constant-velocity case. The differences between the modelled and observed line profiles in the free-expansion case may be related to the omission of Thomson scattering and the simplicity of our quasi-LTE model.

4.4 Overview of the qualitative model

We summarize the main results of the qualitative analysis in a cartoon (Fig. 7). It shows the basic structural elements of SN 1994W which we believe are responsible for the formation of the optical spectrum when the supernova's luminosity is high. The ejecta expand with a velocity of ~ 4000 km s $^{-1}$ into an extended ($\sim 4 \times 10^{14}$ cm) CS envelope. The characteristic density of the CS envelope is $\sim 10^9$ cm $^{-3}$. The SN ejecta are enshrouded by the opaque CDS within which the photosphere resides during most of the luminous phase. The opaque CDS precludes the formation of absorption lines from the ejecta. The CDS presumably forms primarily during shock break-out and is subsequently maintained by both CS material swept up by the radiative forward shock and SN material swept up by the reverse shock. These shocks are not shown in Fig. 7 but they are presumably located at the distances $\Delta R < 0.1R$ away from the outer and inner edges of the CDS.

Attached to the CDS is a layer populated by dense ($n \approx 4 \times 10^{13}$ cm $^{-3}$) fragments supplied by the RT instability of the dense CDS and, possibly, by radiative shocks in CS clouds. This inhomogeneous layer of dense material is the primary site of the broad emission lines with the characteristic velocity of the line-emitting gas, 4000 km s $^{-1}$ (e.g., in He I).

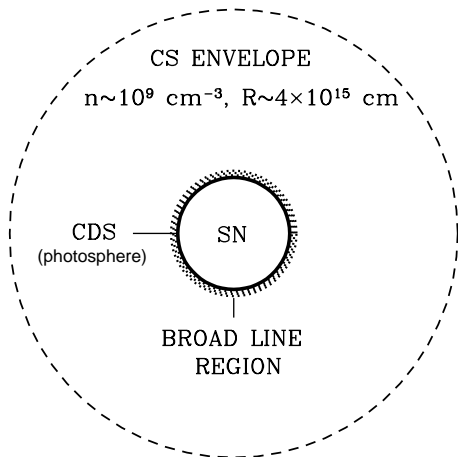


Figure 7. A sketch of SN 1994W at the epoch around day 30. We show the principal structural elements involved in the formation of the spectrum. The SN ejecta are bounded by an opaque cool dense shell (CDS), which is responsible for the continuum radiation. The broad-line region is a narrow mixing layer attached to the CDS, composed of Rayleigh-Taylor fragments of the CDS matter and possibly of shocked CS clouds. The SN ejecta expand into a dense CS envelope with Thomson optical depth on the order of unity. The CS envelope is responsible for both narrow lines and the extended Thomson wings seen in $H\alpha$.

The CS envelope, which in turn expands with a velocity of $\sim 1000 \text{ km s}^{-1}$, is responsible for the narrow lines. Thomson scattering in the CS envelope results in the emergence of broad emission-line wings, which are most apparent in the strong lines such as $H\alpha$ and $H\beta$. Because of the large expansion velocity, the red wing is stronger than the blue wing.

5 A MODEL FOR $H\alpha$

In order to confirm and refine the above qualitative picture of the formation of the SN 1994W spectrum, we have modelled the $H\alpha$ line profile. In many respects our approach repeats the analysis of SN 1998S by Chugai (2001), which involved calculations of the CDS dynamics and Monte Carlo computations of the emergent lines formed outside the CDS. Here we use an updated version of this model, which now includes calculations of CS hydrogen ionization, electron temperature and $H\alpha$ emissivity. In the previous model both of the latter were set rather arbitrarily.

5.1 The model

The CDS dynamics are calculated numerically in the thin-shell approximation (Chevalier 1982). We assume that the SN initially expands homologously ($v \propto r$) with density distribution $\rho = \rho_0/[1 + (v/v_k)^9]$, where the parameters of the distribution are defined by the ejecta mass M and kinetic energy E . At radius $R_0 = 1000 R_\odot$ (a rather arbitrary value)

the SN ejecta begin to interact with the extended stellar envelope. The density of the extended stellar envelope is adjusted in our model by the requirement that a strong initial deceleration of the swept-up thin shell must result in an expansion velocity of $\sim 4000 \text{ km s}^{-1}$ on day 30 when the photospheric radius reaches $\sim 10^{15} \text{ cm}$. The CS envelope is attached to the stellar envelope at $r \approx 10^{15} \text{ cm}$. A constant pre-shock velocity (1000 km s^{-1}) is assumed for the CS gas. This is a reasonable approximation for the homologous expansion, bearing in mind additional radiative acceleration. For the SN mass and energy we adopt $M = 8 M_\odot$ and $E = 10^{51} \text{ erg}$ — both values are close to the parameters of the light-curve models B and C of Falk & Arnett (1977). We find that the dynamical model is nearly the same for SN mass in the range $7\text{--}9 M_\odot$. The evolution of the CDS radius and velocity is shown in Fig. 8 for the density profile which is also consistent with the $H\alpha$ model. In fact, the optimal density is a compromise between the requirements imposed by the $H\alpha$ profile evolution, the CDS velocity, and the bolometric luminosity at the final stage of the light-curve plateau. The density of the CS envelope is nearly flat ($\rho \propto r^{-0.4}$) in the range $10^{15} < r < 4 \times 10^{15} \text{ cm}$.

The ionization of the CS envelope is produced by both X-ray emission from the radiative forward shock wave and by photospheric radiation. The latter primarily operates via hydrogen photoionization from the second level. The X-ray luminosity of the forward shock wave is calculated as

$$L_x = 2\pi r^2 \rho (v_s - u_{ps})^3, \quad (7)$$

where ρ is the pre-shock density, while the pre-shock velocity u_{ps} is the superposition of the pre-explosion velocity and the accelerated velocity term. Half of this luminosity is directed toward the CDS where it is reprocessed into continuum radiation. This component is not treated explicitly in the model. The other half of the X-ray luminosity of the forward shock is emitted outward and is partially absorbed by the CS gas. The X-ray spectrum of the forward shock is approximated as $F_E = CE^{-q} \exp(-E/T_s)$, where T_s is the temperature of the forward shock defined by the shock velocity $v_s - u_{ps}$. The spectral power index $q = 0.5$ roughly describes both the Gaunt factor and the contribution of X-ray lines in the low-energy band (Terlevich et al. 1992). The soft X-rays from the reverse shock at the epoch under consideration are fully absorbed by the CDS (cf. Fig. 9 of Fransson, Lundqvist & Chevalier 1996) and by the SN ejecta, and are reprocessed into the optical.

The energy of the X-rays absorbed in the CS envelope is shared between heating, ionization and excitation. Excitation and ionization by the photospheric radiation are also taken into account. The electron temperature T_e in the CS envelope is determined from the energy balance between heating from ionization by X-rays and photospheric radiation and cooling due to hydrogen. This approximation is quite reasonable in the temperature range of $(1 - 2) \times 10^4 \text{ K}$. The hydrogen atom is treated in the two-level-plus-continuum approximation. The degree of ionization we obtain for hydrogen in the CS envelope lies typically in the range $0.8 - 0.95$. The $H\alpha$ emissivity is due to recombination (Case B) and collisional excitation. Collisional de-excitation of $H\alpha$ is included in the computation of the net emissivity. To allow for uncertainties in the flux, model, distance and reddening we use a fitting parameter C_n for narrow $H\alpha$. This

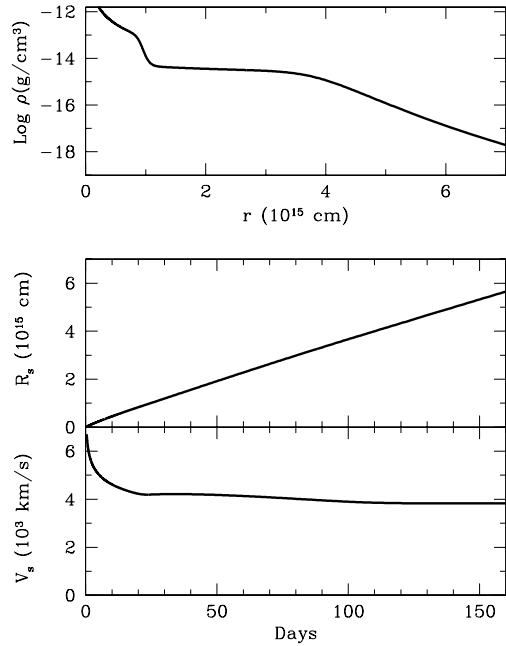


Figure 8. The CS density (*top panel*) and evolution of the radius and velocity of the cool dense shell (*lower panels*).

parameter is a multiplicative factor in the $H\alpha$ emissivity in the CS envelope.

The broad-line region (Fig. 7) is described by an (on average) homogeneous layer, $R_s < r < R_1$, where $R_1/R_s = 1.15$ and the distribution of the line luminosity $dL/dv \propto v$ for $v_1 < v < v_s$, where v_1 is the minimal velocity adopted to be equal to the pre-shock CS gas velocity. We express the average emissivity of the broad component in terms of the pre-shock emissivity, multiplied by a fitting factor C_b , which is restricted by the requirement that the $H\alpha$ intensity from the broad-line region cannot exceed the black-body value for the local electron temperature of the CS gas in the pre-shock zone.

We assume free expansion pre-explosion kinematics ($u = hr$), though we have also explored the constant-velocity case. The acceleration by the SN radiation is described as an additional CS velocity term $u_a = u_0(R_s/r)^2$, where u_0 is a free parameter.

5.2 Thomson scattering and the broad component

In the $H\alpha$ line profile, the broad emission component and electron-scattering wings overlap and at first sight cannot be disentangled unambiguously. Nevertheless, we found that there is not much freedom in the decomposition procedure. In Fig. 9 we show a model narrow-line component on day 31, with the broad component turned off. To emphasize the different behaviours of the broad component and the electron-scattering wings, we show in Fig. 10 models with different Thomson optical depth (0, 1 and 2.8) but with otherwise similar parameters. For optical depth zero, the modelled broad component is strongly skewed toward the blue because of occultation by the photosphere. This asymmetry decreases as τ_T increases and Thomson scattering of the

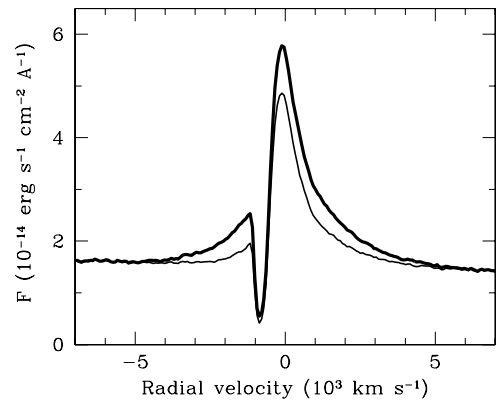


Figure 9. A typical model of $H\alpha$ on day 31 (*thick line*), showing the contribution of the narrow component (*thin line*).

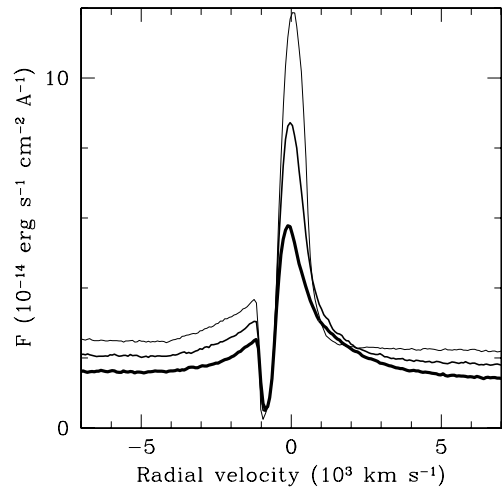


Figure 10. The same model as in Fig. 9 but for different Thomson optical depths. Lines with increasing thickness show cases $\tau_T = 0, 1$ and 2.8 , respectively.

line emission in the expanding CS envelope produces an increasingly strong red wing. These different behaviours of the broad line and electron-scattering wings permit us to disentangle the contribution of the two line components in $H\alpha$. In passing, we note that the continuum level also depends on τ_T , since the Thomson optical depth affects the escape probability of photons emitted by the photosphere.

5.3 $H\alpha$ and the expansion law

The sensitivity of the model line profile to the kinematics of the CS envelope is demonstrated in Fig. 11. The plot shows $H\alpha$ profiles on day 31 computed for similar model parameters — all that differs is the velocity distribution. For $\tau_T = 2.8$, homologous expansion without post-explosion radiative acceleration fits the observations quite well. The

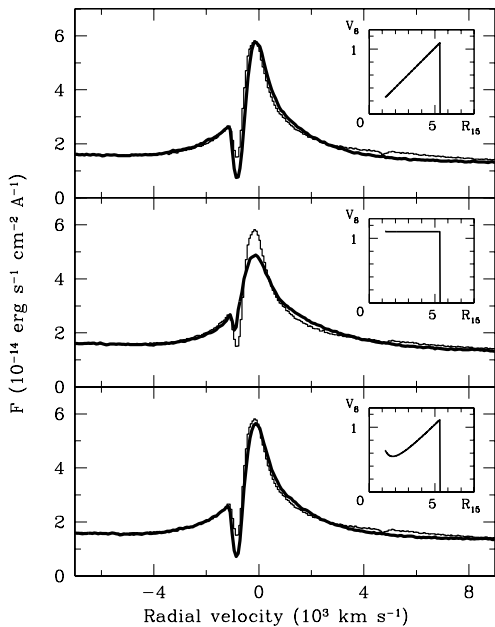


Figure 11. $H\alpha$ profile on day 31 for different velocity distributions (shown in the inset in each panel). Overplotted on each observed profile (*thin line*) are models for CS envelope kinematics displayed in insets.

constant-velocity case is much less successful: it produces an emission component which is too broad, and absorption which is too shallow (Fig. 11). This result, taken together with the results of the narrow CS line modelling (Fig. 6), argues against the constant-velocity case. We checked a model with constant velocity and pre-shock acceleration and found, unsurprisingly, that this gives even worse agreement. The homologous model, on the other hand, works just as well when combined with post-explosion acceleration. In the bottom panel of Fig. 11 we show such a model profile characterized by an amplitude of accelerated velocity term of $u_a = 400 \text{ km s}^{-1}$.

Although homologous expansion kinematics is certainly preferred, this model shows a rather deep absorption component. This contradiction is not related to the finite resolution since we have smoothed the model profile by a Gaussian with appropriate width. An explanation for the large absorption strength in the model might be hidden in a possible deviation of the kinematics from homologous expansion, some clumpiness of the CS envelope, or lower hydrogen excitation in the outer layers of the CS envelope than the model predicts.

5.4 Modelling the $H\alpha$ evolution

We have calculated $H\alpha$ for three epochs (31, 57 and 89 days past explosion) using the density distribution of the CS envelope ($r > 10^{15} \text{ cm}$), and the CDS radius and velocity as shown in Fig. 8. The density parameter $w = 4\pi r^2 \rho$ at $r = 10^{15} \text{ cm}$ on day 31 is $w = 7.5 \times 10^{16} \text{ g cm}^{-1}$. Free expansion kinematics is assumed with a boundary velocity of 1100 km s^{-1} at $r = 5.4 \times 10^{15} \text{ cm}$ on day 31. This implies an age for the CS envelope of $t_{cs} = 1.5 \text{ yr}$ when the SN

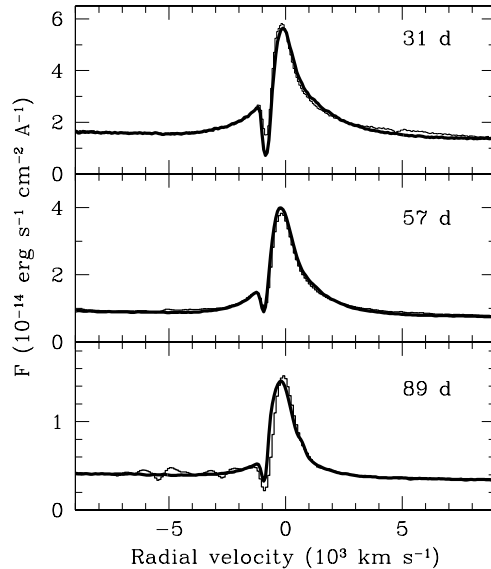


Figure 12. $H\alpha$ at different epochs. Model profiles (*thick line*) are overlaid on the observations (*thin line*).

explodes. For other values of t_{cs} counted from the moment of envelope ejection, we rescale according to $r \propto t_{cs}$ and $\rho \propto 1/t_{cs}^3$.

The computed profiles are shown in Fig. 12. In Table 4 we list the corresponding parameters: photospheric (CDS) radius, photospheric temperature, brightness dilution, CDS velocity, post-explosion velocity increase, and emissivity fitting factors for narrow and broad components. The last column displays the calculated Thomson optical depth outside the CDS. On days 31 and 57 we use the approximation of an opaque photosphere. On day 89 we found, however, that this approximation predicts too weak a red part of the profile. The model agrees better with the observations if we suggest that at this late phase the CDS is semi-transparent. To describe this effect in a simple way we allow a photon striking the photosphere to cross it and escape into the CS medium with a finite probability, which we found should be close to $p = 0.3$. This assumption is qualitatively consistent with the fact that the photospheric brightness on day 89 is diluted ($\xi = 0.2$) for the optimal continuum temperature. The models for all three epochs demonstrate satisfactory fits to the data. On day 31, the model is consistent with the presence of broad He I $\lambda 6678$ in the red wing of $H\alpha$, while on day 57 the model fit in the red wing does not leave any room for the He I line. This behaviour is consistent with the weakening of other He I lines at this time.

We calculated the $H\alpha$ component from the CS envelope in a unified way with a minimum number of free parameters. For this reason, the fact that the tuning parameter of the narrow-line intensity (C_n) is close to unity (Table 4) means that within the uncertainties (~ 20 per cent) the electron distribution in the CS envelope recovered from the Thomson scattering effects is also consistent with the luminosity of the narrow $H\alpha$ component. Because the line luminosity depends on the filling factor as $L \propto 1/f$ while the Thomson optical depth does not, we conclude that the filling factor in the CS

envelope is close to unity in at least most of the line-forming zone.

This last observation is of crucial importance for distinguishing between the two scenarios for the formation of the broad-line region (Section 4.2), and indicates that CS clouds do not play a significant rôle in this process.

We have studied cases with different density power-law indices s (defined via $\rho \propto r^s$) in the flat part of the CS envelope. In the case $s = 0$, the tuning parameter (C_n) must systematically decrease by a factor of 1.25 to fit the profile. For $s = -1$, C_n should systematically increase with time by a similar factor. Bearing in mind the uncertainties in the modelling and fluxing, we do not rule out that the density gradient lies in the range $-1 \leq s \leq 0$.

5.5 Implications for the origin of the circumstellar envelope

The model for the H α evolution presented above for the CS envelope outside $r \approx 10^{15}$ cm argues for a total mass of $M_{cs} \approx 0.4 M_\odot$ and kinetic energy of $E_{cs} \approx 2 \times 10^{48}$ erg. Combined with the derived kinematic age of the CS envelope $t_{cs} \approx 1.5$ yr, the average kinetic luminosity of the mass-loss mechanism responsible for the ejection of the CS envelope then becomes $L \approx E_{cs}/t_{cs} \approx 4 \times 10^{40}$ erg s $^{-1}$, and the average mass-loss rate is $\sim 0.3 M_\odot$ yr $^{-1}$.

The kinetic luminosity we derive here is enormous compared to stellar values. It exceeds by two orders of magnitude the radiative luminosity of a pre-supernova with a main-sequence mass of $\leq 20 M_\odot$. This certainly rules out a superwind as the mass-loss mechanism responsible for the CS envelope around SN 1994W. The CS envelope around SN 1994W must have been born as a result of a rather violent mass ejection initiated by some energetic explosive event in the stellar interior ($E \geq 2 \times 10^{48}$ erg) at ~ 1.5 yr prior to the SN outburst.

6 LIGHT-CURVE MODELLING

To model the broad-band photometric light curves, we use the multi-energy group radiation hydrodynamics code STELLA (Blinnikov et al. 1998, 2000). In the current work, STELLA solves time-dependent equations for the angular moments of intensity averaged over fixed frequency bands, using 200 zones for the Lagrangian coordinate and up to 100 frequency bins with variable Eddington factors. The transfer of gamma rays from radioactive decay is calculated using a one-group approximation for the non-local deposition of the energy of radioactive nuclei. Except for the latest phases, the gamma-ray deposition is not important for SN 1994W. In the equation of state, LTE ionizations and recombinations are taken into account, but radiation is not assumed to be in equilibrium with matter. The effect of line opacity is treated as an expansion opacity according to the prescription of Eastman & Pinto (1993). In comparison with previous work with STELLA, here we use an extended spectral line list, the same as in the discussion of SN 1998S by Chugai et al. (2002).

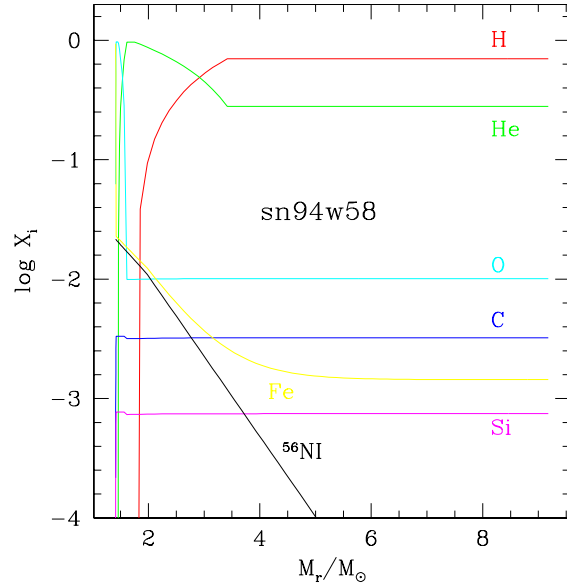


Figure 13. Composition as a function of interior mass, M_r , for the most abundant elements in the pre-supernova model sn94w58. The mass cut is at $M_c = 1.41 M_\odot$.

6.1 Pre-supernova models

SCL98 used analytical fits (Litvinova & Nadyozhin 1983, 1985; Popov 1993) to estimate the pre-SN radius, mass and explosion energy in SN 1994W. However, those fits are only valid for typical SNe II-P, and from the discussion above we know that SN 1994W was instead dominated by circumstellar interaction. To determine the pre-supernova parameters for such an unusual event, we therefore need to do detailed numerical modelling. This can be done only for a subset of the pre-supernova parameters, so we used a cut-and-trial approach, guessing the initial conditions and computing light curves in order to meet the constraints posed by the photometry and the spectral analysis of Section 5. In the absence of an evolutionary model, we built a sequence of several dozens of non-evolutionary models, converging finally on a reasonably good fit to observations. Our initial models are constructed in hydrostatic equilibrium for the bulk mass, while the outer layers mimic the structure of the circumstellar envelope.

For a given mass M and radius R_0 , we obtain a model in mechanical equilibrium assuming a power-law dependence of temperature on density (Nadyozhin & Razinkova 1986; Blinnikov & Bartunov 1993):

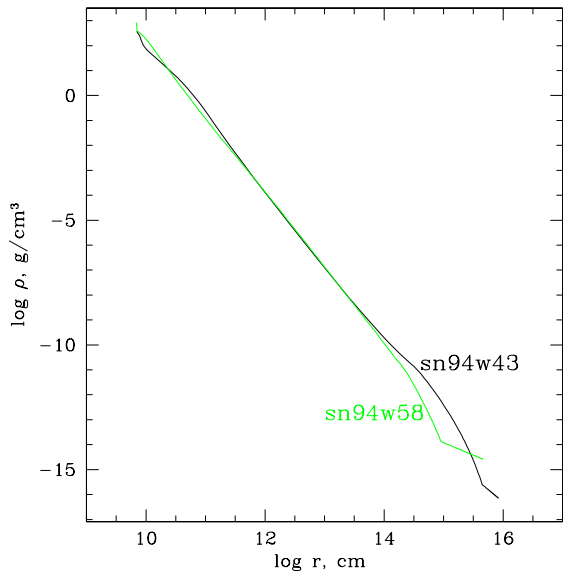
$$T \propto \rho^\alpha. \quad (8)$$

The hydrostatic configuration thus obtained would be close to a polytrope of index $1/\alpha$ if it were chemically homogeneous and fully ionized. The difference from a polytropic model arises due to recombination of ions in the outermost layers and non-uniform composition (Fig. 13).

In the centre of this configuration, at the mass cut of the collapsing core, we assume a “point-like” gravitating hard core (with numerical radius $R_c = 0.1 R_\odot$ — much larger than a real core, but much smaller than the radii of mesh zones involved in our hydrodynamic simulations). The den-

Table 4. Parameters of the H α evolution models

Day	R_p (10^{15} cm)	T (K)	ξ	v_s (km s $^{-1}$)	u_a (km s $^{-1}$)	C_b	C_n	τ_T
31	1.2	16000	1	4220	400	35	1.15	2.8
57	2.2	7760	1	4160	400	1	1	2.0
89	3.3	7000	0.2	3920	170	0.5	1.15	0.54

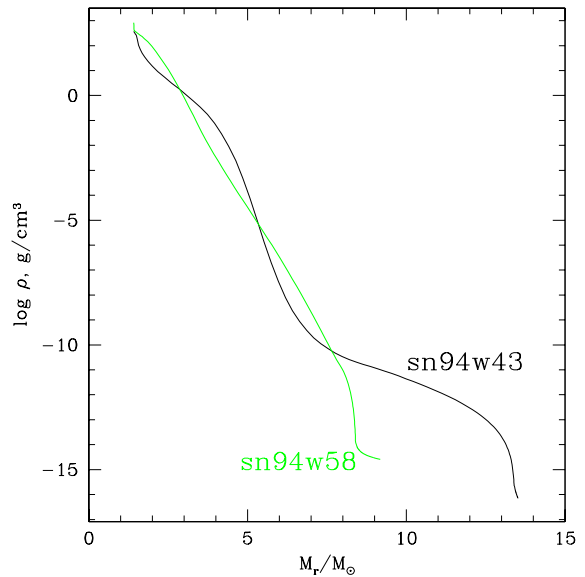
**Figure 14.** Density as a function of the radius r in the pre-supernova models sn94w43 and sn94w58.

sity structure found in this way is shown in Figs. 14 and 15.

The parameters of the models are given in Table 6.1. The first column is the model label, which is followed by the mass of SN ejecta, pre-supernova stellar radius, ^{56}Ni mass, power-law index α , density of the CS envelope (ρ_{15}) at the radius $r = 10^{15}$ cm, power-law index (p) of the CS envelope density distribution $\rho \propto r^{-p}$, the outer radius of the CS envelope, and the kinetic energy at infinity in units of foe (1 foe = 10^{51} erg).

Each model was exploded by the deposition of heat energy in a layer of mass $\sim 0.06 M_{\odot}$ outside of $1.41 M_{\odot}$. Since STELLA does not include nuclear burning, preservation of the same mixed composition in the ejecta is assured.

We explored parameter space for the mass (M) and energy (E) of the SN ejecta and found acceptable fits to the data for masses in the range 6–15 M_{\odot} and with the energy given by the ratio $E/M \approx 0.15\text{--}0.2$ foe M_{\odot}^{-1} . In the following sections and in Table 6.1, we present three representative models which allow us to demonstrate different aspects of the formation of the light curve. Of these three, model sn94w58 provides our best fit to SN 1994W, model sn94w43 shows that a normal SN II-P light curve is not appropriate for SN 1994W, and model sn94w68 illustrates what the supernova light curve might have looked like without CS interaction. All three models have $E = 1.5 \times 10^{51}$ ergs. This energy is typical for good light-curve models. The

**Figure 15.** Density as a function of the interior mass (M_r) in the pre-supernova models sn94w43 and sn94w58. The mass cut is at $M_c = 1.41 M_{\odot}$.

asymptotic kinetic energy of the ejecta is somewhat lower and is given in the Table 6.1.

6.2 Hydrodynamics and shock propagation

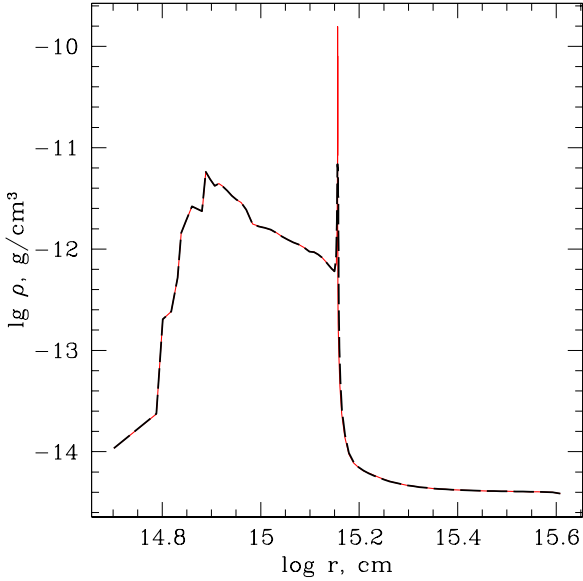
The modelled light curves are dominated by the diffusion of the trapped radiation generated during the shock wave's propagation in the extended stellar atmosphere and subsequent emission of a radiative shock propagating in the dense circumstellar medium. A dense shell is formed which is found in non-equilibrium radiation hydrodynamic modelling but often missed in equilibrium diffusion modelling. We identify this dense shell as the CDS discussed in Section 4.1. The Lagrangian code STELLA does a good job of resolving the very fine structure of the opaque shell, which contains approximately one solar mass of the material (Fig. 16).

6.3 Light curves

In Figs. 17 and 18 we show the changes in the colour temperature, T_c , of the best black-body fit to the flux. We compare this to the effective temperature, T_{eff} , defined by the luminosity and the radius of last scattering R through $L = 4\pi\sigma T_{\text{eff}}^4 R^2$ (see Blinnikov et al. 1998 for details of finding R and from that T_{eff}). Our multi-group radiative trans-

Table 5. Parameters of hydrodynamical models

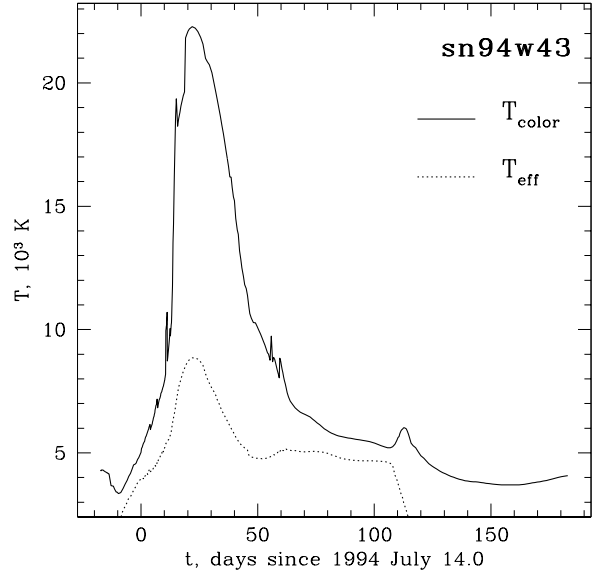
Model	M_{ej}^a (M_{\odot})	R_0 ($10^4 R_{\odot}$)	M_{Ni} (M_{\odot})	α	ρ_{15} ($10^{-15} \text{ g cm}^{-3}$)	p	R_w ($10^4 R_{\odot}$)	E_{kin}^b (10^{51} erg)
sn94w43	12	8	0.015	0.319	5	2	12	1.07
sn94w58	7	2	0.015	0.31	12	1	6.6	1.25
sn94w64	7	2	0.015	0.31	0	-	-	1.33

^a pre-supernova mass = $M_{\text{ej}} + 1.41 M_{\odot}$ ^b kinetic energy at infinity**Figure 16.** Density as a function of radius (r) in two models with different amounts of artificial smearing at day 30. The height of the density spike with small smearing (*solid line*) reaches the theoretical estimate for an isothermal shock wave.

fer with hydrodynamics obtains this temperature in a self-consistent way, and no additional estimates of the thermalization depth are needed (in contrast to the one-group model of Ensmann & Burrows 1993, for example). The large difference between colour and effective temperatures is partly due to a geometric effect (the radius of last scattering is greater than the effective radius of photon creation) and partly due to the blanketing effect of scattering (the average energy of the photons is higher than that corresponding to the value of T_{eff} ; Schuster 1905). The modelled T_c changes in a way similar to the values derived from black-body fits to the spectra (Section 3.2.3).

The light curves are shown in Figs. 19, 20 and 21. The model sn94w43 produces a bright light curve, but the second half of its plateau is dominated by diffusion, not by the shock, so the behaviour of colours is similar to that of a typical SN II-P.

The density of the more powerful wind in the model sn94w58 follows the law $\rho \propto r^{-1}$. This model produces a much better fit to the colours at the late plateau phase. The flat CS density distribution is consistent with the modelling

**Figure 17.** Colour and effective temperatures for the model sn94w43. Realistic, scattering-dominated opacity has been assumed. The solid line shows the temperature of the best black-body fit to the flux (colour temperature). The dashed line shows the effective temperature defined by the luminosity and the radius of last scattering.

of H α evolution (Section 5.4). Model sn94w64, which is exactly the same as model sn94w58 in the bulk mass, but does not have the powerful wind, is much less luminous at the late plateau phase. This shows the importance of CS interaction for the luminosity.

The time-dependence of the radius R_s and velocity V_s of the cool dense shell in model sn94w58 is shown in Fig. 22. The two nearly indistinguishable lines in the V_s plot are obtained by taking $V_s = dR_s/dt$ numerically, and by taking the mass-averaged speed of matter inside the shell. A comparison with Fig. 8 shows good agreement with the spectral model, although V_s is somewhat higher in the hydrodynamical model. The difference is at most ~ 10 per cent.

To summarize, the hydrodynamical modelling of the light curve of SN 1994W suggests that the optimal light curve is produced in a model which contains a dense CS envelope at $r \gtrsim 10^{15} \text{ cm}$ with a relatively flat density distribution and an outer radius of $\sim 4.5 \times 10^{15} \text{ cm}$. This conclusion is fully consistent with the H α modelling.

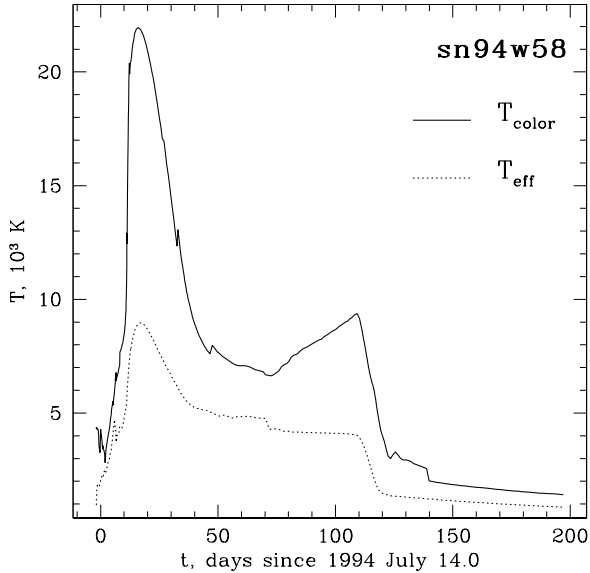


Figure 18. Colour and effective temperatures for the model sn94w58.

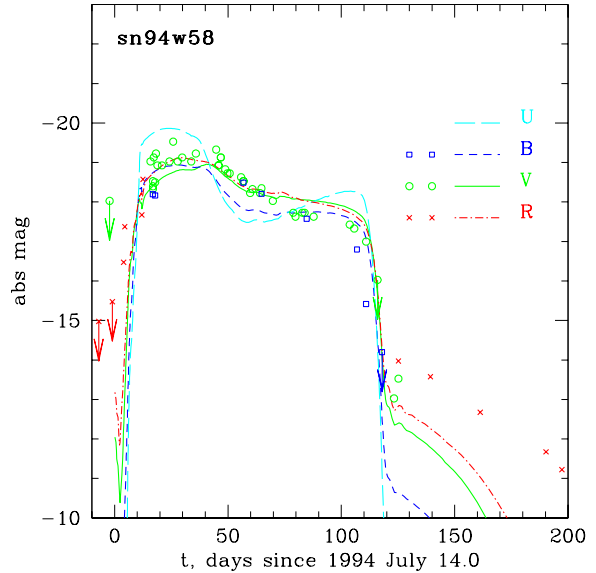


Figure 20. Same as in Fig. 19, but for model sn94w58.

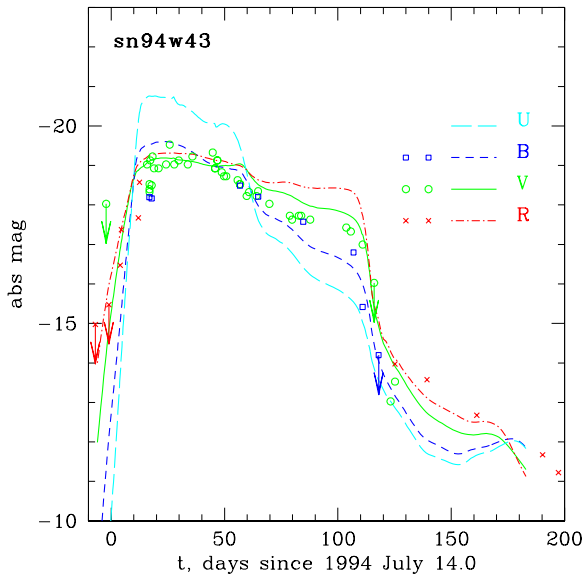


Figure 19. Light curves for the model sn94w43. The photometric points are taken from SCL98 and references therein.

7 DISCUSSION AND CONCLUSIONS

We have presented and analysed spectra and light curves of SN 1994W, one of the best-observed SNe IIn. During the first three months the spectrum clearly shows the presence of three line components: (i) narrow P-Cygni lines, (ii) intrinsically broad lines and (iii) extended smooth wings in $H\alpha$ and $H\beta$. We attribute these components, respectively, to (i) a dense CS envelope, (ii) shocked, cool, dense gas confined in a narrow layer on top of the photosphere, and (iii) the effects of Thomson scattering in the CS envelope.

Our line profile analysis and hydrodynamical light-curve modelling have led us to a coherent picture. SN 1994W

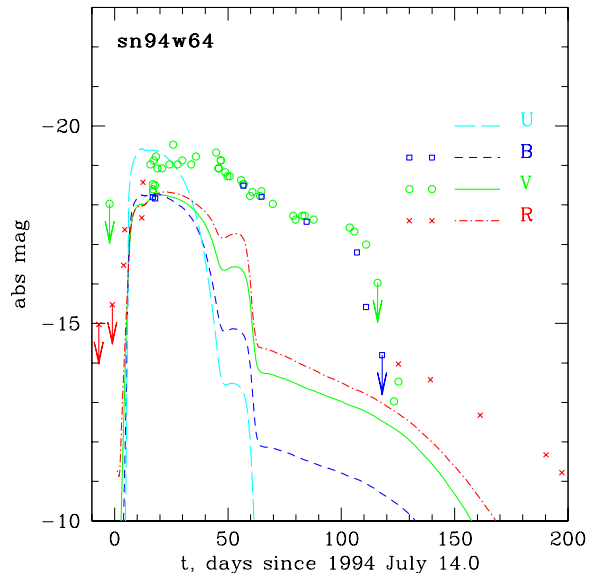


Figure 21. Same as in Fig. 19, but for model sn94w64.

appears to have been the result of explosion of an extended pre-supernova ($\sim 10^{15}$ cm) embedded in an extended CS envelope [$\sim (4 - 5) \times 10^{15}$ cm] with Thomson optical depth ~ 2.8 one month after the explosion.

Although we do not rule out the presence of a wind from a normal red supergiant pre-supernova outside the dense CS envelope, such a wind component cannot have been very dense, considering the low luminosity of $H\alpha$ on day 203 ($L \approx 10^{38}$ erg s $^{-1}$). This luminosity is two orders of magnitude lower than for SN 1979C ($\sim 10^{40}$ erg s $^{-1}$) at ~ 1 yr (Chevalier & Fransson 1985). Attributing this difference to the difference in the interaction luminosity ($L \propto 4\pi\rho v_s^3$), we can estimate the density parameter of the outer wind in SN 1994W. The expansion velocity of the CDS in SN 1994W, ~ 4000 km s $^{-1}$, is half that of SN 1979C (~ 8000 km s $^{-1}$).

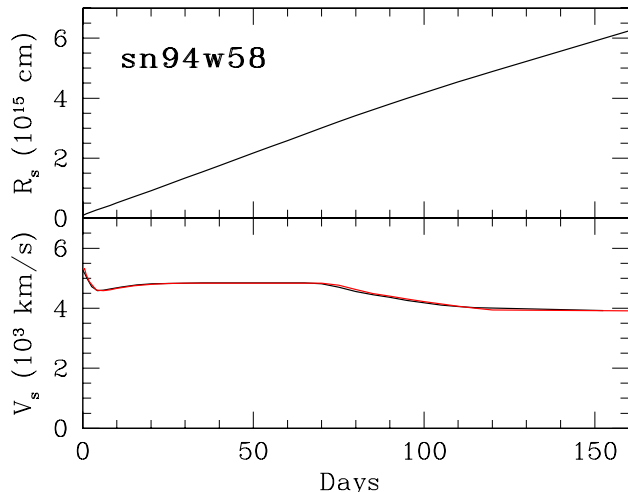


Figure 22. The evolution of the radius and velocity of the cool dense shell in hydrodynamical model sn94w58. Compare with Fig. 8.

Given the SN 1979C wind parameter, $w \approx 10^{16} \text{ g cm}^{-1}$, the outer wind in SN 1994W should have $w \approx 10^{15} \text{ g cm}^{-1}$ to account for the difference in the $\text{H}\alpha$ luminosity. This is at least ten times lower than in SN 1979C, and a factor of two lower than in SN 1980K (e.g., Lundqvist & Fransson 1988). In this respect, the detection by Schlegel (1999) of X-rays from SN 1994W at $t = 1180$ days with luminosity $L \approx 8 \times 10^{39} \text{ erg s}^{-1}$ appears odd when compared with the expected X-ray luminosity ($\lesssim 10^{38} \text{ erg s}^{-1}$) at that epoch for a case of SN/wind interaction with $w \approx 10^{15} \text{ g cm}^{-1}$. To resolve this problem, one would need the wind density to be at least of factor of ten higher at $\sim 4 \times 10^{16} \text{ cm}$, i.e., exceeding that of SN 1979C. This could argue for a possible multi-shell ejection scenario prior to the explosion.

The recovered kinematics, density and linear scale of the CS matter around SN 1994W imply a kinematic age for the CS envelope of $t_{\text{cs}} \approx 1.5 \text{ yr}$, mass $M_{\text{cs}} \approx 0.4 M_{\odot}$ and kinetic energy $E_{\text{cs}} \approx 2 \times 10^{48} \text{ erg}$. The enormous average mass-loss rate ($M_{\text{cs}}/t_{\text{cs}} \approx 0.3 M_{\odot} \text{ yr}^{-1}$) and equally enormous kinetic luminosity ($E_{\text{cs}}/t_{\text{cs}} \approx 4 \times 10^{40} \text{ erg s}^{-1}$) of the mass-ejection mechanism strongly suggest that the CS envelope has been lost as a result of an explosive event which occurred $\sim 1.5 \text{ yr}$ prior to the SN outburst.

In their model for the narrow lines in SN 1983K, Grasberg & Nadyozhin (1986) invoked the violent ejection of the hydrogen envelope 1–2 months before the SN explosion with a velocity on the order of $\sim 2500 \text{ km s}^{-1}$ and an energy $(1-2) \times 10^{49} \text{ erg}$. Dramatically high mass loss shortly before explosion has also been derived for the SNe IIn 1995G by Chugai & Danziger (2003), on the basis of an analysis similar to the one we have presented here.

The mechanism behind such violent ejections might be associated with a nuclear flash in the degenerate core of the pre-supernova. This conjecture, also presented by Chugai & Danziger (2003), is prompted by the prediction of Weaver & Woosley (1979) that the O/Ne/Mg core of an

$\sim 11 M_{\odot}$ star may produce strong Ne flashes several years prior to the SN explosion and that the strongest flash could eject most of the hydrogen envelope with velocities of $\sim 100 \text{ km s}^{-1}$. Although such flashes do not occur in more recent models with finer zoning (Woosley, Heger & Weaver 2002), we believe that the effect warrants further investigation, especially given the highly complicated nuclear burning regime and hydrodynamics of degenerate O/Ne/Mg cores.

Remarkably, the low ^{56}Ni mass ($< 0.015 M_{\odot}$) estimated from the tail R -band luminosity of SN 1994W (SCL98) seems to be in accord with the suggested mass of such a progenitor, if at the lower end of our estimated mass range. Such stars are expected to eject only small amounts of ^{56}Ni (Mayle & Wilson 1988). Our models are, however, not very sensitive to the zero-age main-sequence mass of the progenitor, and, as SCL98 point out, the low nickel content could indicate either a low-mass progenitor which may have lost a few solar masses in shell and wind ejections, or a more massive star that lost several solar masses prior to the ejection of the CS shell. Deep X-ray searches for more extended CS material could help solve this problem, as should more detailed models for stellar evolution just prior to core collapse.

How common are events like SN 1994W? Of the SNe IIn that have been observed so far, it is possible that a close counterpart has been seen but not recognised as such due to sparser temporal coverage or greater distance. Nevertheless, several objects have shown narrow hydrogen and Fe II absorption lines with velocities of about 1000 km s^{-1} . This family includes SNe 1987B (Schlegel et al. 1996), 1994aj (Benetti et al. 1998), 1994ak (Filippenko 1997), 1995G (Pastorello et al. 2002), 1996L (Benetti et al. 1999) and 1999el (Di Carlo et al. 2002). We suggest that in at least some of these SNe, a CS envelope was ejected in a violent, explosive manner, as we believe was the case for SN 1994W, and as Chugai & Danziger (2003) have suggested for SN 1995G. Further data and analyses are needed, however, before it can be demonstrated that the energy of the ejected CS envelope is comparable for these events.

In any case, we suggest that at least part of the variety of SNe IIn has been accounted for. Some, like SN 1988Z and SN 1998S, have a dense, slow CS envelope formed by a slow superwind. Others, like SN 1994W, seem to have ejected a CS envelope in a violent event a few years before the SN explosion.

ACKNOWLEDGEMENTS

We thank Aaron J. Barth, Mike Breare, René Rutten, Luis C. Ho, Neil O’Mahony, Chien Y. Peng and Ed Zuiderwijk for helping take observations for us, and Clive Jackman, Danny Lennon and Marco Azzaro for help assessing the day 31 spectrum calibration. We also thank Itziar Aretxaga, Eddie Baron, Claes Fransson, Seppo Mattila, Peter Meikle, Miguel Pérez Torres, and Luca Zampieri for discussions.

This paper is based on observations made with the Isaac Newton Telescope (INT), the William Herschel Telescope (WHT), and the Nordic Optical Telescope (NOT). The INT and WHT are operated on the island of La Palma by the Isaac Newton Group in the Spanish Observatorio del Roque de los Muchachos of the Instituto de Astrofísica de Canarias. The NOT is operated on the island of La Palma jointly

by Denmark, Finland, Iceland, Norway, and Sweden, in the Spanish Observatorio del Roque de los Muchachos of the Instituto de Astrofísica de Canarias. Some of the data presented herein were obtained at the W.M. Keck Observatory, which is operated as a scientific partnership among the California Institute of Technology, the University of California and the National Aeronautics and Space Administration. The Observatory was made possible by the generous financial support of the W.M. Keck Foundation.

This project was supported by the Royal Swedish Academy of Sciences. S.I.B. was supported partly by RFBR 02-02-16500, the Wenner-Gren Science Foundation, MPA Garching and ILE Osaka guest programs. The research of P.L. is sponsored by the Royal Swedish Academy and the Swedish Research Council, and he is a Research Fellow at the Royal Swedish Academy supported by a grant from the Wallenberg Foundation. A.V.F.'s research is supported by National Science Foundation grant AST-0307894.

REFERENCES

- Allen, C. W., 1973, *Astrophysical Quantities*. University of London, Athlone Press, London
- Aretxaga, I., Benetti, S., Terlevich, R. J., Fabian, A. C., Cappellaro, E., Turatto, M., Della Valle, M., 1999, *MNRAS*, 309, 343
- Axelrod, T., 1980, Ph.D. thesis, California Univ., Santa Cruz
- Almog, Y., Netzer, H., 1989, *ApJ*, 238, 57
- Benetti, S., Cappellaro, E., Danziger, I. J., Turatto, M., Patat, F., Della Valle, M., 1998, *MNRAS*, 294, 448
- Benetti, S., Turatto, M., Cappellaro, E., Danziger, I. J., Mazzali, P. A., 1999, *MNRAS*, 305, 811
- Bessell, M. S., 1999, *PASP*, 111, 1426
- Blinnikov, S. I., Bartunov, O. S., 1993, *A&A*, 273, 106
- Blinnikov, S. I., Eastman, R., Bartunov, O. S., Popolitov, V. A., Woosley, S. E., 1998, *ApJ*, 496, 454
- Blinnikov, S., Lundqvist, P., Bartunov, O., Nomoto, K., Iwamoto, K., 2000, *ApJ*, 532, 1132
- Blondin, J. M., Ellison, D. C., 2001, *ApJ*, 560, 244
- Bowen, D. V., Roth, K. C., Meyer, D. M., Blades, J. C., 2000, *ApJ*, 536, 225
- Bragaglia, A., Munari, U., Barbon, R., 1994, *IAU Circ.*, No. 6044
- Cardelli, J. A., Clayton, G. C., Mathis, J. S., 1989, *ApJ*, 345, 245
- Chevalier R.A., 1982, *ApJ*, 258, 790
- Chevalier R.A., Blondin J.M., 1995, *ApJ*, 444, 312
- Chevalier R. A., Fransson C., 1985, in Bartel N., ed., *Supernovae as Distance Indicators*, Springer-Verlag, Berlin, p. 123
- Chevalier, R. A., Fransson, C., 1992, *ApJ*, 395, 540
- Chevalier, R. A., Fransson, C., 1994, *ApJ*, 420, 268
- Chugai, N. N., 1990, *Sov. Astr. Lett.*, 16, 457
- Chugai, N. N., 1992, *SvA*, 36, 63
- Chugai, N. N., 1997, *Ap&SS*, 252, 225
- Chugai, N. N., 2001, *MNRAS*, 326, 1448
- Chugai N. N., Blinnikov, S. I., Fassia, A., Lundqvist, P., Meikle, W. P. S., Sorokina, E. I., 2002, *MNRAS*, 330, 473.
- Chugai, N. N., Danziger, I. J., 2003, *Astr. Lett.*, 29, 732
- Cortini, G., Villi, M., 1994, *IAU Circ.*, No. 6042
- Cumming, R. J., Lundqvist, P., Meikle, W. P. S., 1994, *IAU Circ.*, No. 6057
- Di Carlo, E., et al., 2002, *ApJ*, 573, 144
- Dopita, M. A., Evans, R., Cohen, M., Schwarz, R. D., 1984, *ApJ*, 287, L69
- Eastman, R. G., Pinto, P. A., 1993, *ApJ*, 412, 731
- Elitzur, M., Ferland, G. J., Mathews, S. G., Shields, G. A., 1983, *ApJ*, 272, L55
- Ensmann, L., Burrows, A., 1992, *ApJ*, 393, 742
- Fassia, A., et al., 2001, *MNRAS*, 325, 907
- Falk, S. W., Arnett W. D., 1977, *ApJS*, 13, 515
- Filippenko, A. V., 1982, *PASP*, 94, 715
- Filippenko, A. V., 1989, *AJ*, 97, 726
- Filippenko, A. V., 1991, in Danziger, I. J., Kj  r, K., eds, *Supernova 1987A and Other Supernovae ESO*, Garching, p. 343
- Filippenko, A. V., 1997, *ARA&A*, 35, 309
- Filippenko, A. V., 2000, in Holt, S. S., Zhang, W. W., eds, *Cosmic Explosions*, AIP, New York, p. 123
- Filippenko, A. V., Barth, A. J., 1994, *IAU Circ.*, No. 6046
- Filippenko, A. V., Moran, E. C., 1998, *IAU Circ.*, No. 6830
- Fransson, C., 1982, *A&A*, 111, 140
- Fransson, C., 1984, *A&A*, 133, 264
- Fransson, C., Lundqvist, P., Chevalier, R. A., 1996, *ApJ*, 461, 993
- Fransson, C., et al., 2002, *ApJ*, 572, 350
- Fransson, C., et al., 2004, *ApJ*, submitted
- Fuhr, J. R., Martin, G. A., Wiese, W. L., 1988, *J. Phys. Chem. Ref. Data* 17, Suppl. 4
- Gaskell, C. M., 1994, *IAU Circ.*, No. 6048
- Garc  a-Lario, P., Riera, A., Manchado, A., 1999, *ApJ*, 526, 854
- Germany, L., Reiss, D. J., Sadler, E. M., Schmidt, B. P., Stubbs, C. W., 2000, *ApJ*, 533, 320
- Grasberg, E. K., Imshennik, V. S., Nadyozhin, D. K., 1971, *Ap&SS*, 10, 28
- Grasberg, E. K., Nadyozhin, D. K., 1986, *Sov. Astr. Lett.*, 12, 68
- Gualandi, R., Merighi, R., 2001, *BFOSC (Bologna Faint Object Spectrograph & Camera) Manuale Utente*, version 2.0. Osservatorio Astronomico di Bologna, Bologna
- Hamuy, M. et al., 2003, *Nat*, 424, 651
- Henry, R. B. C., Branch, D., 1987, *PASP*, 99, 112
- King, D. L., 1985, *ING Technical Note*, 31
- Klein, R. I., McKee, C. F., Colella, P., 1994, *ApJ*, 420, 213
- Leibundgut, B. et al., 1991, *ApJ*, 372, 531
- Leonard, D. C., Filippenko, A. V., Barth, A. J., Matheson, T., 2000, *ApJ*, 536, 239
- Lewis, J. R., et al., 1994, *MNRAS*, 266, L27
- Litvinova, I. Yu., Nadyozhin, D. K., 1983, *Astrophys. Sp. Sci.* 89, 89
- Litvinova, I. Yu., Nadyozhin, D. K., 1985, *Pis'ma Astron. Zh.* 11, 351 (*Sov. Astron. Lett.* 11, 145)
- Lundqvist, P., Fransson, C., 1988, *A&A*, 192, 221
- Matheson, T., Filippenko, A. V., Ho, L. C., Barth, A. J., Leonard, D. C., 2000, *AJ*, 120, 1499
- Meikle, W. P. S., Catchpole, R. M., Cumming, R. J., Geballe, T. R., Lewis, J. R., Martin, R., Walton, N. A., 1994, *Spectrum*, 4, 7
- Mayle, R., Wilson, J. R., 1988, *ApJ*, 334, 909
- Miller, J. S., Stone, R. P. S., 1993, *Lick Obs. Tech. Rep.*, No. 66

- Murray, C. A., 1983, *Vectorial Astrometry*. Adam Hilger, Bristol
- Nadyozhin, D. K., Razinkova, T. L., 1986, *Nauchnye informatsii*, 61, 29
- Niemela, V. S., Ruiz, M. T., Phillips, M. M., 1985, *ApJ*, 289, 52
- Oke, J. B., et al., 1995, *PASP*, 107, 375
- Pastorello, A., Turatto, M., Benetti, S., Cappellaro, E., Danziger, I. J., Mazzali, P. A., Patat, F., Filippenko, A. V., Schlegel, D. J., Matheson, T., 2002, *MNRAS*, 333, 27
- Pikelner, S. B., 1954, *Izv. Krymsk. Astroph. Obs.* 12, 93
- Popov, D. V., 1993, *ApJ*, 414, 712
- Pozzo, M., Meikle, W. P. S., Fassia, A., Geballe, T., Lundqvist, P., Chugai N. N., Sollerman, J., 2004, *MNRAS*, in press (astro-ph/0404533)
- Rigon, L., Turatto, M., Benetti, S., Pastorello, A., Cappellaro, E., Aretxaga, I., Vega, O., Chavushyan, V., Patat, F., Danziger, I. J., Salvo, M., 2003, *MNRAS*, 340, 191
- Rupen, M. P., et al., 1987, *AJ*, 94, 61
- Ryder, S., Staveley-Smith, L., Dopita, M., Petre, R., Colbert, E., Malin, D., Schlegel, E., 1993, *ApJ*, 416, 167
- Schlegel, E. M., 1990, *MNRAS*, 244, 269
- Schlegel, E. M., Kirshner, R. P., Huchra, J. P., Schild, R. E., 1996, *AJ*, 111, 2038
- Schlegel, E. M., 1999, *ApJ*, 527, 85
- Schuster, A., 1905, *ApJ*, 21, 1
- Shortridge, K., 1990, *Starlink User Note*, 86, Rutherford Appleton Laboratory
- Sigut, T. A. A., Pradhan, A. K., 2003, *ApJS*, 145, 15
- Sollerman, J., Cumming, R. J., Lundqvist, P., 1998, *ApJ*, 493, 933
- Stathakis, R. A., & Sadler, E. M., 1991, *MNRAS*, 250, 786
- Terlevich, R. J., Tenorio-Tagle, G., Franco, J., Melnick, J., 1992, *MNRAS*, 255, 713
- Turatto, M., Cappellaro, E., Danziger, I. J., Benetti, S., Gouffes, C., Della Valle, M., 1993, *MNRAS* 262, 128
- Turatto, M., Suzuki, T., Mazzali, P. A., Benetti, S., Cappellaro, E., Danziger, I. J., Nomoto, K., Nakamura, T., Young, T. R., Patat, F., 2000, *ApJ*, 534, L57
- van Hoof, P., 1999, *Atomic Line List v2.04*, <http://www.pa.uky.edu/~peter/atomic/>
- Wade, R. A., Horne, K., 1988, *ApJ*, 324, 411
- Weaver, T. A., Woosley, S. E., 1979, *BAAS*, 11, 724
- Wegner, G., Swanson, S. R., 1996, *MNRAS*, 278, 22
- Williams, G. A., Shipman, H. L., 1988, *ApJ*, 326, 738
- Woosley, S. E., Heger, A., Weaver, T. A., 2002, *RvMP*, 74, 1015
- Woosley, S. E., 1986, in Hauck B., Maeder, A., Meynet, G., eds, *Nucleosynthesis and Stellar Evolution*, Saas-Fee Advanced Course 16, Geneva Observatory, Sauverny, p. 1